Tijdschrift van het NERG

DE VERENIGING NERG

Het NERG is een wetenschappelijke vereniging die zich ten doel stelt de kennis en het wetenschappelijk onderzoek op het gebied van de elektronica, signaalbewerking, communicatie- en informatietechnologie te bevorderen en de verbreiding en toepassing van die kennis te stimuleren.

BESTUUR

prof.dr.ir. W.C. van Etten, voorzitter
prof.dr.ir. P. Regtien,
    vice-voorzitter
ir. E. Bottelier, secretaris
P.F. Maartense, penningmeester
dr.ir. A.B. Smolders,
    tijdschrift-manager
dr.ir. Tj.J. Tjalkens,
    programma-manager
ir. R.J. Kopmeiners, web-beheer
vacature, onderwijs-commissaris
vacature, ledenwervings-manager

LIDMAATSCHAP

Voor het lidmaatschap wende men zich via het correspondentie-adres tot de secretaris of via de NERG website: http://www.nerg.nl. Het lidmaatschap van het NERG staat open voor hen, die aan een universiteit of hogeschool zijn afgestudeerd en die door hun kennis en ervaring bij kunnen dragen aan het NERG. De contributie wordt geheven per kalenderjaar en is inclusief abonnement op het Tijdschrift van het NERG en deelname aan vergaderingen, lezingen en excursies.

De jaarlijkse contributie bedraagt voor gewone leden € 43,- en voor studentleden € 21,50. Bij automatische incasso wordt € 2,- korting verleend. Gevorderde studenten aan een universiteit of hogeschool komen in aanmerking voor het studentlidmaatschap. In bepaalde gevallen kunnen ook andere leden, na overleg met de penningmeester voor een gereduceerde contributie in aanmerking komen.

HET TIJDSCHRIFT

Het tijdschrift verschijnt vijf maal per jaar. Opgenomen worden artikelen op het gebied van de elektronica, signaalbewerking, communicatie- en informatietechnologie. Auteurs, die publicatie van hun onderzoek in het tijdschrift overwegen, wordt verzocht vroegtijdig contact op te nemen met de hoofdredacteur of een lid van de Tijdschriftcommissie.

Toestemming tot overnemen van artikelen of delen daarvan kan uitsluitend worden gegeven door de tijdschriftcommissie. Alle rechten worden voorbehouden.

TIJDSCHRIFTCOMMISSIE

INHOUD

Van de voorzitter

Wim van Etten
tel: 053-893872 (overdag) of 053-4304837 ('s-avonds)
email: etten@ ieee.org

c)))

URSI en het NERG

Van 17 tot en met 24 augustus l.l. werd in Maastricht de 27ste General Assembly (GA) van de URSI (Union Radio-Scientifique Internationale) gehouden. Dat deze wereldwijde en gezaghebbende organisatie dit jaar haar drie-jarige conferentie in Nederland hield, is te danken aan de inspanning van de toenmalige voorzitter van het Nederlandse URSI-comité, prof. Frans Sluijter. Tijdens de vorige assembly (Toronto 1999) heeft hij Nederland met Maastricht hiervoor kandidaat gesteld en met verve bepleit. Ik kan u verzekeren, dat daarnaast heel wat en tactvol lobbywerk nodig is, om het zover te krijgen, dat de kandidatuur ook daadwerkelijk wordt toegewezen, want meerdere landen willen maar wat graag zo'n conferentie in huis halen. Ook in 1999 was dat het geval, met o.a. onze grote Oosterbuur als belangrijke concurrent.

Toen de toewijzing eenmaal een feit was, heeft Sluijter vervolgens ook zich tot taak gesteld om de organisatie van de URSI GA te gaan leiden, als voorzitter van de organisatiecommissie. Dat hij daartoe het voorzitterschap van het Nederlandse URSI-comité opgaf, na deze functie vele jaren vervuld te hebben, lag voor de hand.

De URSI is georganiseerd langs lijnen van nationale vertegenwoordigingen "Member Committees" genaamd, voor Nederland dus het Nederlands URSI-comité. Dit is een comité van het NERG, conform onze Statuten en Huishoudelijk Reglement. In de meeste landen, echter, ressorteren de nationale comités onder een "KNAW-achtige" organisatie. Toen Nederland zich aansloot bij URSI, in de twintiger jaren van de vorige eeuw, toonde de KNAW hier te lande echter geen belangstelling voor die rol. Een van de kopstukken van het radio-onderzoek in Nederland in die tijd was Balthasar van der Pol. Bovendien was die ongeveer terzelfder tijd betrokken bij de oprichting van het NRG, later NERG geheten. De link naar het NRG was uit dien hoofde dus voor de hand liggend, en zo is het dus zo'n 80 jaar gebleven.

Tot nu toe is er slechts eenmaal eerder een URSI GA in Nederland georganiseerd geweest, dat was in 1954 in den Haag, en dan nu dus voor de tweede maal. Het was een buitengewoon succesvolle conferentie, met veel voordrachten, posters, een tentoonstelling en uitreiking van een aantal prestigieuze prijzen. De presentaties zijn opgedeeld langs de lijnen van de zogenaamde "commissions" (10 stuks), die variëren van propagatie, via radio-astronomie tot signalen en systemen. In feite lopen er dus 10 conferenties parallel. Er waren van Nederlandse zijde in totaal 35 bijdragen (mondelinge presentaties en posters) van verschillende onderzoeksinstituten, voorwaar niet gering. In de categorie van de prijswinnaars moet vermeld worden, dat de "Balthasar van de Pol"-prijs werd toegekend aan onze landgenoot prof. dr. ir. Aad de Hoop, bij u allen waarschijnlijk wel bekend. De uitreiking werd verricht door een kleinzoon van van der Pol.

Naast de inhoudelijke kant van de conferentie, verliep de organisatie, waarin ondergetekende namens het NERG zitting had, vrijwel vlekkeloos. Frans Sluijter, die al zo'n 30 jaar binnen URSI actief is, had als voorzitter van de organisatiecommissie de zaken voortreffelijk voor elkaar: streng waar dat nodig was, soepel waar dat kon en altijd vriendelijk. Hij had bovendien een door de wol geverfde organisatiecommissie bijeengebracht. Het lijkt me hier gepast, om Frans en alle commissieleden hiervoor namens het NERG van harte bedanken voor de uitstekende organisatie van dit grootse evenement.

In samenwerking met het Nederlandse URSI-comité gaat het NERG binnenkort een Themabijeenkomst organiseren, waar een aantal van de Nederlandse bijdragen voor u nog eens worden gepresenteerd.

17ᵉ General Assembly van het URSI

Bart Smolders
Voorzitter NERG redactie
E-mail: redactie@nerg.nl

Maastricht, MECC

Net na de zomervakantie (17-24 Augustus) werd in het conferentiecentrum van het MECC in Maastricht de General Assembly van het URSI gehouden. Dit wetenschappelijk evenement wordt om de drie jaar georganiseerd en kon ook dit maal weer rekenen op een groot aantal deelnemers (+/- 1400) vanuit alle windstreken. Tot nu toe zijn er 17 General Assembly's gehouden, waarvan nu tweemaal in Nederland. In 1922 werd de eerste General Assembly georganiseerd en wel in Brussel. Het URSI heeft zijn oorsprong in België, waar men met name in radio geïnteresseerd was voor het onderhouden van verbindingen vanuit het moederland met de koloniën [1]. Het is dan ook niet verwonderlijk dat het secretariaat van het URSI nog steeds in België zit. Verder is het opvallend dat alle communicatie vanuit het URSI nog steeds tweetalig is, zowel de Engelse- als de Franse taal wordt gebruikt. Dit laatste geeft het URSI wellicht een meer 'wetenschappelijke' uitstraling dan organisaties zoals IEEE.

De eerste keer dat er een General Assembly in Nederland werd georganiseerd was in 1954 en wel in Den Haag. Het gebeurt dus maar maximaal eenmaal in je wetenschappelijke carrière dat dit evenement in Nederland wordt gehouden. Op zich dus een zeer bijzondere gebeurtenis voor de Nederlandse radio-gemeenschap. Voor het URSI in Nederland tevens een mooie gelegenheid om zich te profileren en om met name bij jonge ingenieurs meer bekendheid te krijgen. Wellicht sterker nog dan het NERG heeft de Nederlandse URSI gemeenschap te maken met een vergrijzing onder haar leden.

Sinds het ontstaan van het URSI (Union Radio-Scientifique Internationale) in 1919 zijn er een tiental commissies opgericht, welke ieder een bepaald aspect van het radio-vakgebied behandelt. De tien commissies zijn:

A. Elektromagnetische metrologie
B. Velden en golven

Figuur 1: Beurs waarin instituten en bedrijven hun kennis en producten konden uitdragen
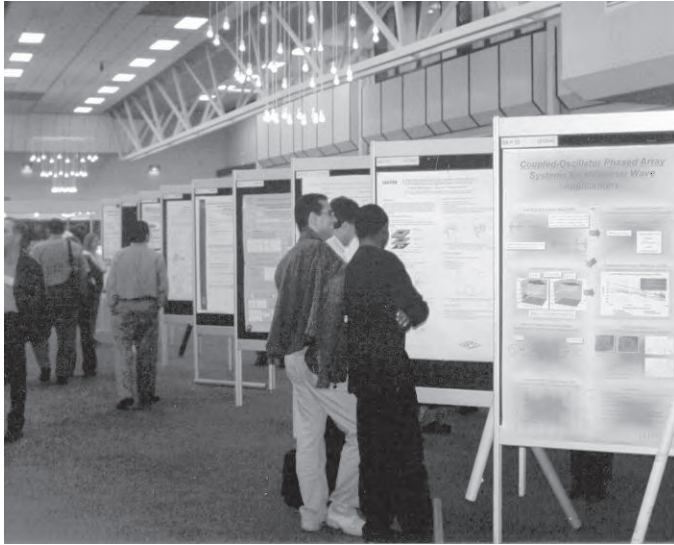
Figuur 2: Poster sessies

C. Signalen en systemen
D. Elektronica en Fotonica
E. Elektromagnetische ruis en interferentie
F. Golfvoortplanting en aardobservatie
G. Interactie van radiogolven met de ionosfeer
H. Golven in plasma's
J. Radioastronomie
K. Elektromagnetisme in biologie en geneeskunde

Figuur 3: Presentatie tijdens wetenschappelijke sessie.

Het programma van de General Assembly is opgedeeld in een vijftal activiteiten, te weten: wetenschappelijke voordrachten (oral sessions), tutorials, algemene voordrachten, posters en een beurs waar een beperkt aantal bedrijven en instituten te zien waren. Iedere commissie organiseert een aantal sessies, soms in samenwerking met een andere commissie, waardoor er continue een groot aantal parallelle sessies zijn. Verder werden er tijdens de week ookdiverse sociale activiteiten georganiseerd. De foto's op deze en de vorige pagina geven een impressie van het geheel.

De Nederlandse inbreng was dit jaar aanzienlijk. Er zijn meer dan 40 voordrachten gehouden door medewerkers van een Nederlands instituut of bedrijf, onder meer door bijdrages van alle Technische Universiteiten en van de Universiteit Groningen. Verder een grote inbreng van ASTRON en bijdrages van FEL-TNO, KPN, NMI en ESA-ESTEC. Verder waren er ook diverse posters van Nederlandse komaf. Opvallend is de grote inbreng uit het vakgebied radio-astronomie, vanuit Nederland getrokken door ASTRON. Het URSI is voor deze groep van wetenschappers duidelijk het belangrijkste platform voor kennisuitwisseling.

In dit nummer van het NERG Tijdschrift zullen we ruim aandacht geven aan de Nederlandse inbreng tijdens de General Assembly. We hebben daartoe een 11-tal artikelen geselecteerd die we in dit nummer geplaatst hebben. We hebben hierbij zoveel mogelijk geprobeerd om een uniforme verdeling te vinden over de verschillende commissies en over de bijdrages van de diverse instituten, bedrijven en universiteiten. Voor meer informatie over de General Assembly en over andere URSI activiteiten kunt U kijken op de website: www.ursi-ga2002.nl.
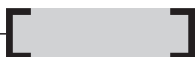
Referenties

[1] Frans W. Sluijter
    "URSI in Maastricht, 17-24 Augustus 2002"
    Tijdschrift van het NERG, nr. 2, p. 76, 2002.

Photonic beamforming for phased-array radar

F.E. van Vliet
TNO-FEL, P.O.Box 96864, 2509JG, The Hague, The Netherlands
Tel: +31.70.374.07.40, Fax: +31.70.374.06.54, Email: vanvliet@fel.tno.nl

Introduction

Future radar systems will increasingly be applying electronically steered arrays. The re-use of apertures for different applications, including communication and electronic support applications, is a key issue. The scarcity in antenna locations poses further advantages to antenna co-location or antenna sharing. The sharing of antenna apertures by different systems implies that the antenna, including the front-end and beamformer, has to cover the full bandwidth of the systems it has to serve. This requirement is in agreement with a further increase in bandwidth of the individual systems, in order to improve performance. A relative bandwidth per system between one and two octaves is targeted.

This system approach brings a number of problems. One of the important problems is the bandwidth of the active antenna. This bandwidth issue plays for both the antenna element, the transmit/receive module components and for the beamformer. The alternatives for beamforming are RF beamforming, IF beamforming, digital beamforming, optical beamforming and hybrid beamforming. Of these alternatives, optical beamforming offers potentially the highest bandwidth, and may hence solve the squinting problem, normally present in large wideband antennas. Figure 1, shown below, illustrates how serious the squinting problem can be by relating the mispointing angle with the beamwidth. For this reason, optical beamforming has been subject of study over the last years at TNO-FEL. This paper summarises the Dutch results and achievements in the field of optical beamforming for electronically steered arrays.

Non-coherent optical TTD beamforming

The wideband potential of optical beamforming is most clear from the possibility of making wideband switched true-time delays (TTD). Due to the fact that the RF signal has a negligible relative bandwidth as compared to the optical carrier, the

Figure 1. Theoretical beam squint as a function of array size.
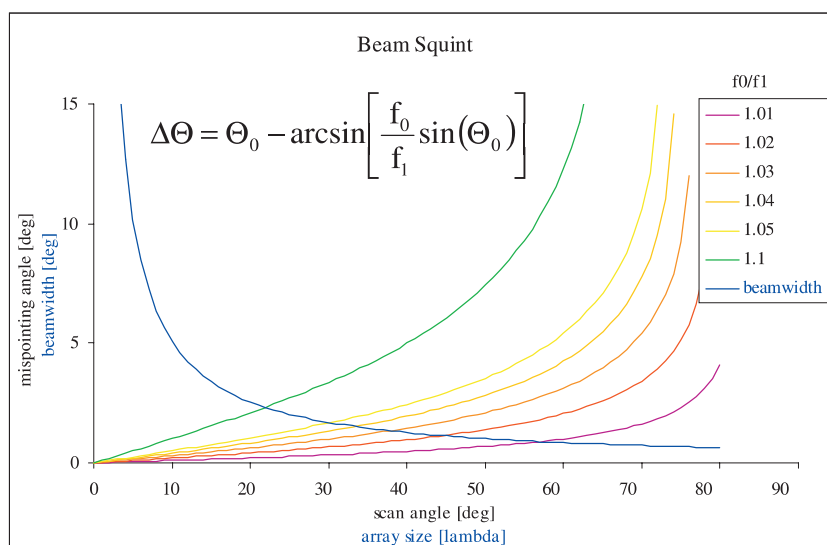
Figure 2. Photo of 4-channel optical beamformer (left) with the antenna pattern results (right). The beamformer was characterised together with ASTRON.

bandwidth limitations will be based on the electronic interfaces. Several TTD beamformers and beamforming architectures have been demonstrated. Technologies that were demonstrated include discrete delay lines in the form of fibres as well as integrated delay lines on SiO2 and InP. For the switches, both elect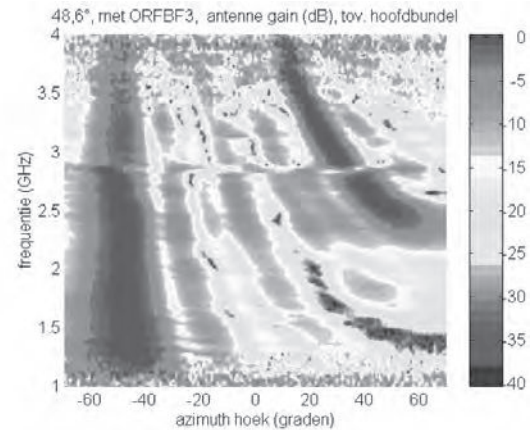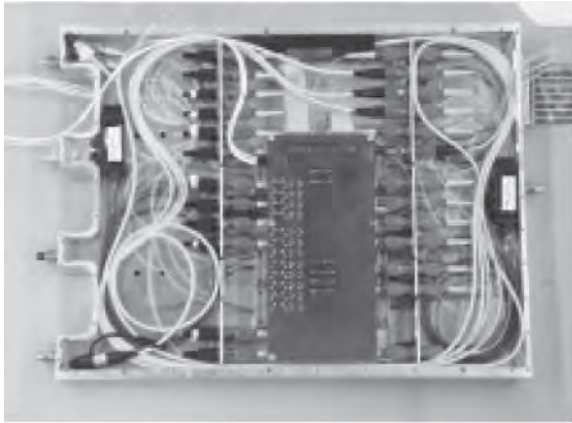ro-optic as well as thermo-optic switches have been applied. Each of these technologies has advantages for particular time delays needed or for specific switching time requirements.

In co-operation with ASTRON, TNO-FEL has developed a four-channel optical true-time delay beamformer. This beamformer is based purely on telecommunications components with directly modulated lasers, and is suitable for systems where the switching speed between different beams is in the order of milliseconds. The demonstrated performance of the beamformer is a dynamic range of 101 dB Hz^(2.3) over an octave bandwidth (2 to 4 GHz).

Figure 3. Photograph of the 4-beam Rotman lens beamformer
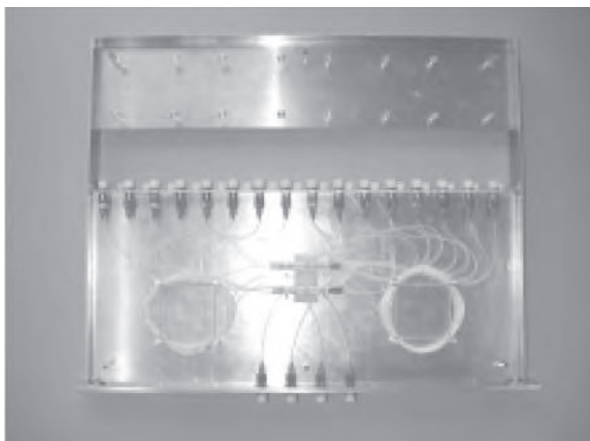
Furthermore, we have recently designed a fiber-optic Butler matrix. The insertion loss is identical to the insertion loss for a single-beam beamformer, the extra beams are obtained by using the additional outputs of the optical splitters. The beamformer offers four outputs corresponding to individual beams and is shown in Figure 3. The beamformer realises 0, 10, 22.5 and 45 degrees beam patterns. It will be demonstrated at a subsystem level in the near future.

Coherent optical beamforming using an OPLL source and OEIC technology

Coherent beamforming can inherently offer more dynamic range to optical links than non-coherent beamformers. Disadvantages for coherent beamformers include the need for a coherent optical source, the need for polarisation-maintaining components and an increased sensitivity to vibration and thermal variations.

To overcome these limitations, an optically coherent source has been developed, operating at 2.5 GHz. This source, based on the optical phase-locked loop (OPLL) principle, incorporates two semiconductor lasers and microwave electronics that locks the two sources together with the help of a reference source. The difference between the two laser signals then copies the accuracy of the reference source into the optical domain. The OPLL exhibited a locking range of 700 MHz and a locking time of several hours.

In co-operation with the Delft University of Technology an integrated coherent beamformer on InP has been designed and tested. The OEIC incorporates 16 channel phase and amplitude control and
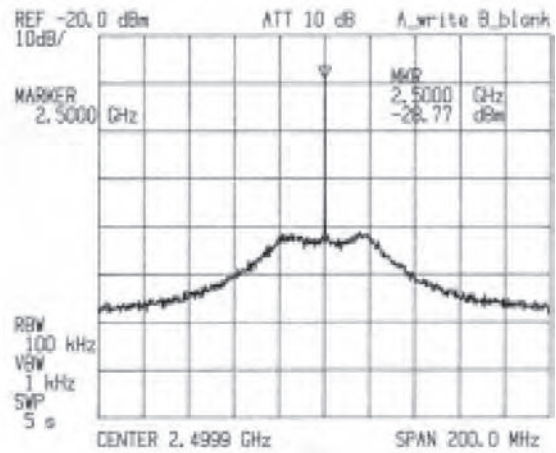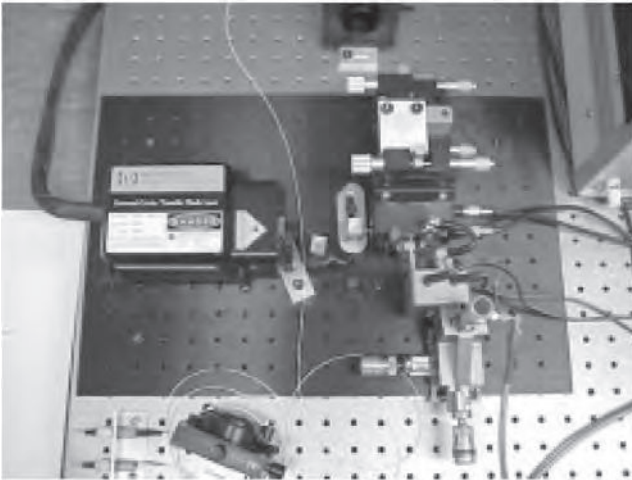
Figure 4. Test set-up of the OPLL and the spectrum measured.

requires the OPLL to be functional. Measurement results show that more than 360 degrees phase control can be obtained and up to almost 20 dB attenuation. A four-channel beamformer was developed as a derivative.

Conclusion

In conclusion, recent developments have resulted in optical beamformers that can provide very wideband beamforming solutions capable of providing more than 100 dB Hz^(2/3) dynamic range. The beamformers presented show state-of-the-art performance. They can be based on telecommunication components for non-coherent beamforming. The results achieved indicate that optical technology is ready to be applied in wideband electronically steered arrays. Depending on the application, non-coherent beamforming is currently the preferred method, due to the insensitivity to the set-up to vibration and environmental conditions.

Figure 5. Photograph of the 16-channel InP beamforming OEIC
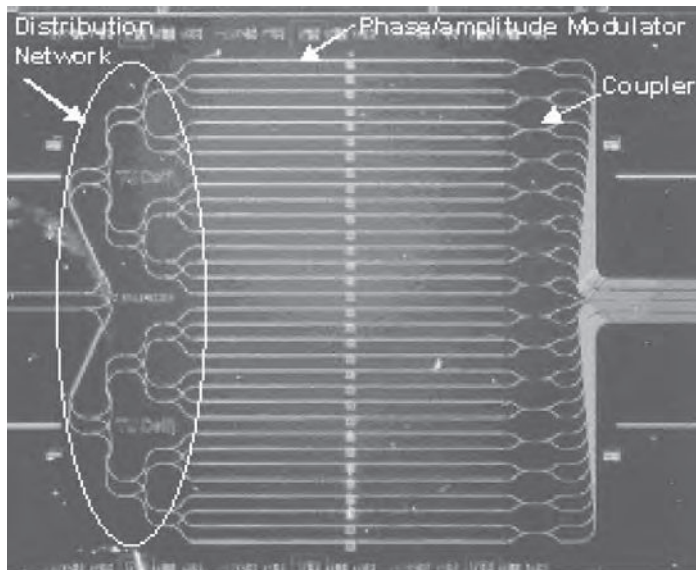
Deformation measurement with repeat pass airborne interferometry[1]

J.S. Groot
TNO-FEL, P.O. Box 96864 2509 JG 's-Gravenhage,
The Netherlands

Abstract

River dikes can deform and eventually burst due to extreme high water conditions. This deformation should be measurable with repeat pass SAR interferometry. An experiment with the PHARUS SAR was carried out to verify this. Two flights were carried out with 5.5 days in between them. During the data acquisition on the second day the dike was deliberately deformed. Interferogram analyses showed that the dike deformed by at most 2 mm on this day, in approximate agreement with tachymeter measurements. Unfortunately, the coherence of the interferograms formed by the data of the separate days was too low to measure deformation.

Introduction

Due to extreme high tide river dikes can lose their stability. This is forewarned by increasing deformation which should therefore be monitored. Conventional deformation measurements (e.g. levelling) are point measurements, and are in addition costly and time consuming. The objective of this work was to demonstrate the capability of airborne SAR interferometry to measure cm-level deformations (spaceborne SAR cannot be used because of the low revisit rate). In order to reach this goal two measurement flights were carried out with the PHARUS C-band SAR [1], while a small dike segment was forced to deform during the second flight.

The experiment

Two flights were performed on 12 and 18 September 2001[2]. The dike was imaged about 10 times during each of these with ~15 minutes in between the images. The flying height was 6000 m, and the incidence angle at the dike 55 degrees. All images were processed to about 1.2 m azimuth and 5.1 m slant range resolution.

Two corner reflectors were put on the deforming dike segment, another two for reference purposes on nearby stable land. On 18-9 the dike was forced to deform by pumping water underneath it and loading it with concrete blocks, all during high tide. In addition the hinterland was dug off. Reflector levelling showed a downward deformation of 5-7 mm between 12-9 and 17-9, and 19 mm between 17-9 and 18-9 (the measurements were done some time before and after pumping). This proves that the pumping etc. of 18-9 was effective.

The perpendicular baseline of every pair of images is less than a few tens of meters. This implies a coherence loss below ≈10 % due to baseline decorrelation. Azimuthal beam steering was not initialised correctly, which implied some coherence loss which varies with the aircraft attitude.

Interferogram analysis

Four interferograms were analysed, which are discussed in the next sections:

1. Run 1/7 of 18-9 (≈ 2.5 hour time span). This interferogram includes part of the deformation induced on 18-9. Moreover, the interferogram will have a high coherence due to the short time span.

2. Run 1/3 of 12-9 (≈ 27 minute time span). This interferogram should exhibit no deformation, because no deformation was caused on this day. It is used as a check for interferogram 1.

3. Run 1 12-9 / run 1 18-9 and run 3 12-9 / run 1 18-9 (≈ 5.5 day time span). These interferograms should reveal about 5 mm deformation (deduced from corner reflector levelling).

---

2   For brevity's sake 12-9 and 18-9 will refer to the two measurement dates from here onwards.
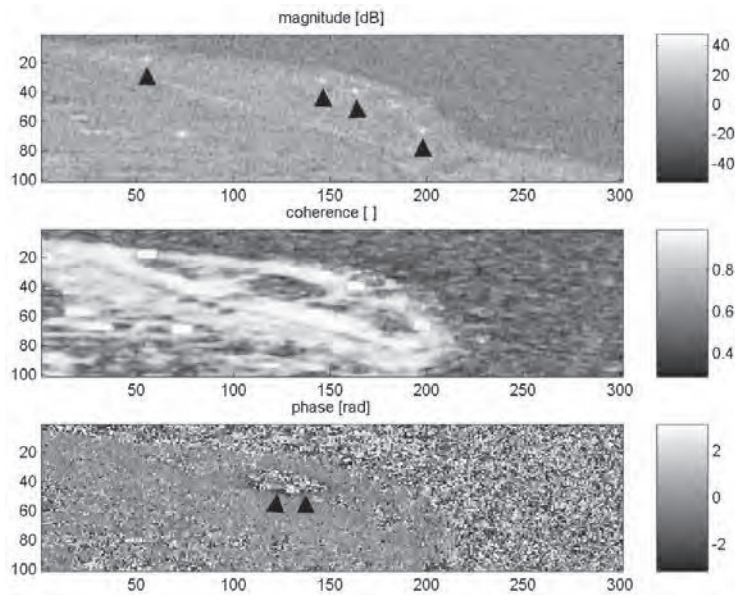
Fig. 1. From top to bottom: magnitude (in dB's), coherence and phase (rad) of the test area. The images are 330 m in azimuth (which increases from left to right) and 300 m in slant range (which increases from top to bottom). The river Lek is at the top (low coherence, noisy phase).

The Run 1/7 18-9 Interferogram

Fig. 1 shows the magnitude, coherence and phase of this interferogram. It is a subsection of the larger 10 km squared interferogram.

The corner reflectors are indicated by the four black rectangles in the magnitude image. The middle two ones are near the borders of the test area (measuring only 70 m × 50 m) which was deformed.

The coherence image shows that the dike with reflectors has a coherence near 0.9, while the area behind the dike (the hinterland) is incoherent (coherence of about 0.4. This rather high value is due to the small template size). This area was dug off to make deformation more probable. It was therefore lower than the surrounding area and quite moist, with puddles occurring at many places. This caused the low coherence.

At first sight the phase image at the bottom shows no signs of deformation, because it is fairly homogeneous. This is in seeming disagreement with the fact that i) it was forced to deform by pumping etc. and ii) the levelling results of the two reflectors on the dike. The only hint at deformation is the black border around the non-coherent area in the hinterland, indicated by the two black triangles. Comparison of the phases of the centre two reflectors to those of the (stable) outer reflectors led to the conclusion that the centre reflectors had changed in height by at most ± 2 mm, which confirms the absence of any substantial deformation.

Tachymeter data was available at some 50 positions in the test area for about every 20 minutes. These were used to compute a map of the radial deformation. This map was co-registered to the interferometric phase image (a subsection of Fig. 1) by using the surveyed reflectors. The result is shown in Fig. 2.

The map at the bottom shows an area of deformation with a maximum of some 7 cm. The red dots indicate the two corner reflectors located on the dike, which exhibited 5 ± 2 mm deformation according to the tachymeter data (the levelling results that indicated 19 mm dike deformation cover a larger time span than this interferogram). This is in

Fig. 2. Comparison of interferometric phase (top) and tachymeter data (bottom). Deformations are in meters (see greyscales at the right).
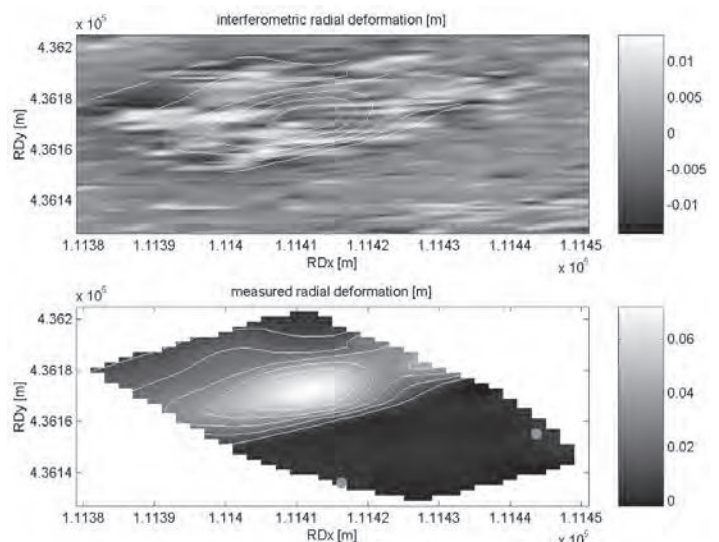
approximate agreement with the 2 mm derived from the interferogram. The yellow contour lines are copied to the phase image at the top for easy reference. A remarkable fact of the phase image is that the incoherent (noisy phase) area corresponds (almost) exactly to the deforming area. On the other hand, the dike and its immediate surroundings are coherent. The incoherence of the hinterland is due to the water on the surface. At the top left of the phase image is a dark patch (the black border in the phase image of Fig. 2) which seems to be coherent. The deformation corresponding to the patch's phase is in approximate agreement with the tachymeter measurements.

The Run 1/3 12-9 Interferogram

This interferogram looks quite similar to the one of run 1/7 of 18-9. Corner reflector response analysis gave that the accuracy of deformation measurement with PHARUS is about ±2 mm if reflectors are used.

Fig. 3 compares the coherence of the test area on 12-9 and 18-9. The black arrow (in the 18-9 coherence image) indicates that the hinterland (which was coherent at 12-9) was incoherent at 18-9. This shows that we simply had bad luck on 18-9. Otherwise the coherence images are quite similar.

The Run 1 12-9/Run 1 18-9 and Run 3 12-9/Run 1 18-9 Interferograms

The coherence of both these interferograms is too low to derive deformation information. This lack of coherence can be due do imaging errors (i.e., a too large baseline) or temporal decorrelation. The ERS SAR (also C-band) coherence of grassland can easily be above 0.5 for a 30 day temporal baseline. However, it will be smaller if the weather conditions are bad during or near the acquisitions, as was the case for the second flight over the river Lek. Further analysis of the flight should reveal what the real cause of the low coherence is.

Conclusions

An experiment with the PHARUS C-band SAR was carried out to measure dike deformation. Two flights were carried out with 5.5 days in between them. Although the dike deformed by a few centimetres between 17-9 and 18-9 interferogram analysis showed that the deformation during the 18-9 interferogram time interval was at most 2 mm. This was approximately confirmed by tachymeter data (5 ± 2 mm). The coherence of the interferograms formed by the data of the separate days was too low to measure deformation.

Reference

[1] P. Snoeij, P. Hoogeboom, P.J. Koomen, B.C.B. Vermeulen, H. Pouwels, "Design and calibration of the PHARUS polarimetric airborne SAR", *2nd Int'l Airb. Remote Sensing Conf.*, 24-27 June 1996, San Francisco

Fig. 3. Coherence of the test area and its surroundings on 12-9 (top) and 18-9 (bottom; see also Fig. 1). The two white rectangles near coordinates (150,40) indicate the positions of the two corner reflectors put in the test area, on the dike.
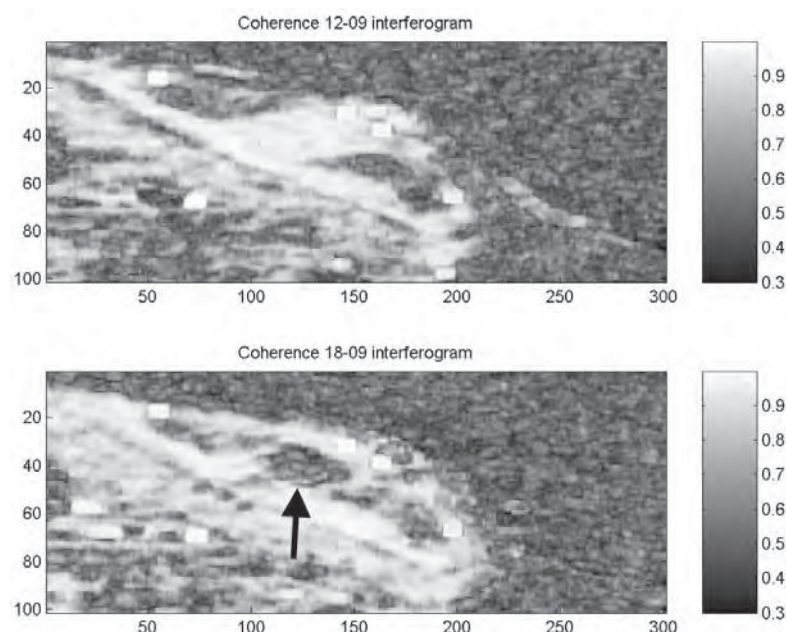
First celestial measurement results of the Thousand Element Array

J. G. Bij de Vaate [(1)] *, G.W. Kant* [(2)] *, W.A. van Cappellen* [(3)] *, S. van der Tol* [(4)]
ASTRON, Oude Hoogeveensedijk 4, 7991 PD, Dwingeloo, The Netherlands
E-mail: vaate@astron [(1)] *, kant@astron.nl* [(2)] *, cappellen@astron.nl* [(3)] *, tol@astron.nl* [(4)]

Abstract

A phased-array demonstrator known as the Thousand Element Array (THEA) is currently under construction of which the first celestial results with a single tile are presented in this paper. THEA is an out-door phased array system that is able to detect signals from different strong astronomical sources simultaneously (multi-beaming). It consists of sixteen one square meter tiles (arrays) operating in the frequency band of 600-1700MHz. The beamforming for THEA is done at two levels; Radio Frequency (RF) beamforming on every tile (64 elements) and digital beamforming with the sixteen tiles [1]. A sky image shows satellite detection in the RF signal. The sun is detected with the auto correlator back-end

Introduction

The international radio-astronomy community is currently making detailed plans for the development of a new radio telescope: the Square Kilometer Array (SKA). This instrument will be two orders of magnitude more sensitive than telescopes currently in use. ASTRON is in the process of establishing phased array technology, which is particular attractive for the 200-2000MHz frequency range of SKA. For this a number of prototype systems have been build, an 8-element Adaptive Array Demonstrator (AAD) and a 64-element One Square Meter Array (OSMA)[2]. Phased arrays have the advantage of multi-beaming and interference rejection - both of major interest in current radio astronomy. Multiple beams not only allow more users on the system at the same time, but also create possible observations which cannot be done with traditional instruments. Each THEA tile can form two independent RF-beams from which 32 finer dependent digital beams can be formed when the signals of the 16 tiles are combined in the digital

beamformer. Adaptive digital beamforming has been implemented.

Implementation

Front-end

The antenna element designed for THEA is a taper slot Vivaldy element with a close to two octaves wide bandwidth[3]. The antenna is followed by a Low Noise Amplifier (LNA) with a 40 Kelvin Noise Temperature at room temperature. After the LNA the signal is splitted to create the two beams. A Vector Modulator subsequently takes care of the Phase and Amplitude modulation. RF combining networks create the RF signal, which is down converted and digitized with 40MHz 12 bits Analogue to Digital Convertors. The digital output of each beam is transmitted to the THEA back-end with a 1.2Gb/sec fiber link.

The tile, realized for THEA, is a low cost casted epoxy structure. Fig.1 gives a photograph of 4 tiles, covered with a radome. Besides the tile also compact low cost has been pursued with the design of units as the column board, containing the antenna, LNA and Vectormodulators, and the IF receiver unit. For all these parts, multiplayer boards have been designed that combine the RF electronics, the digital control electronics and the power supply distribution. The column board e.g. is a 8 layer board with 2 microstrip layers on the outsides (two times signal and ground) and 4 layers inside for power supply and control. For the connection to the row board a single multipurpose connector has been used. Fig. 2 give a picture of the board. With these board designs a significant step has been made in direction of low cost front-ends that are affordable on the SKA scale. The parameters of the dual receiver chain are controlled with a Front-End Controller (FEC). The FEC sets the vectormodula-

Fig. 1. Four THEA tiles in a compact setting, covered with the protecting radome

Fig. 2. A picture of a column board, with 4 antennas, amplifying and beamforming network

tors on the columnboards and the parameters for the receiver unit. It is capable of the storage of 1200 pre-calculated beams, which allows fast beam switching, of interest for the deterministic nulling of moving interferes e.g. satellites. For the power supply of all the units, a DC-DC convertor has been used. It creates the required voltages out of a 48 DC supply.

Back-end

In the (digital) data processing of the THEA, two major parts can be distinguished, see also the blockdiagram in fig. 3: the Adaptive Digital Beamformer (ADBF) and the Reduction and Acquisition unit (RAP). The ADBF consists of the Adaptive Weight Estimator (AWE) and the actual digital beamformer. The RAP consist of a memory / beam selection board and a digital signal processing board.

The incoming 1.25Gbit/s serial data stream on the fibers is converted to parallel on the High Speed Link (HSL) receiver. In order to handle the resulting parallel lines, up to 400, a high density connector is used in combination with a dense
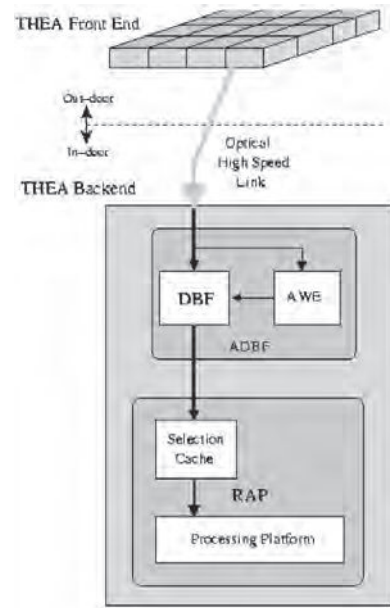
Fig. 3. Block diagram of the THEA system

'sandwich' structure: the HSL fiber receiver board is plugged directly on the DBF while the DBF is placed on top of the RAP unit, fig.4 gives a picture of the three boards. The complete assembly is mounted in an industrial PC in a standard PCI slot. The final output of the system is then stored on a hard-disk or on storage CD's.

The Digital Beamformer is controlled by the AWE. The AWE determines from snapshots of the raw data the optimal, in terms of RFI suppression, complex weights of the DBF. For RFI studies and multi-beam experiments, memory has been placed on the selection board. With this memory 16 channels (beams) can be stored for 0.8 seconds or one channel for 12 seconds.

The processing unit performs a 1024 points FFT. The number of integrations can be set with a

Fig. 4. Photograph of the High Speed Link Receiver, the Digital Beamformer and the Selection board

minimum of 32 spectra (100µs) and a maximum of 4000 spectra (100ms). With post processing the integration time can be enlarged up to 1hour. The processing unit is capable of performing autocorrelations of two channels simultaneously or complex cross correlations of two independent channels, with a bandwidth of 20MHz.

System test

A first quarter of THEA (4 tiles) has been produced. Calibration of a phased array system is a crucial step. For this a Phase Toggling Technique has been developed [4]. The verification of such processes was traditionally only possible by measuring beam patterns. However, the calibration accuracy of each individual element could be verified using a Planar Near Field Scanner. With the scanner, data are taken and transferred into a holographic view of the aperture of the array. Additionally the scanner data are transferred to provide far field beam patterns [5].

Since the indoor measurements are on a single tile level in an artificial environment, a re-calibration is required when tiles are combined and placed outside. In particular, truncation effects change the antenna behavior [6]. A reference source, placed in a nearby mast, has been used to perform a re-calibration at the antenna platform, again using the phase toggling technique.

Results

A strong far field source in the THEA band is the recently launched digital radio satellite. Afristar transmits a carrier with modulation at 1480MHz. The satellite is geo stationary and could in principle be used for the calibration of the system as well. Fig. 5 shows the signal levels at 1480MHz of one tile, where the satellite shows up at 26° elevation and 165° azimuth. Some basic array aspects are demonstrated with this measurement. Due to the spacing of the array, $\lambda/2$ for 1200MHz, on a rec-
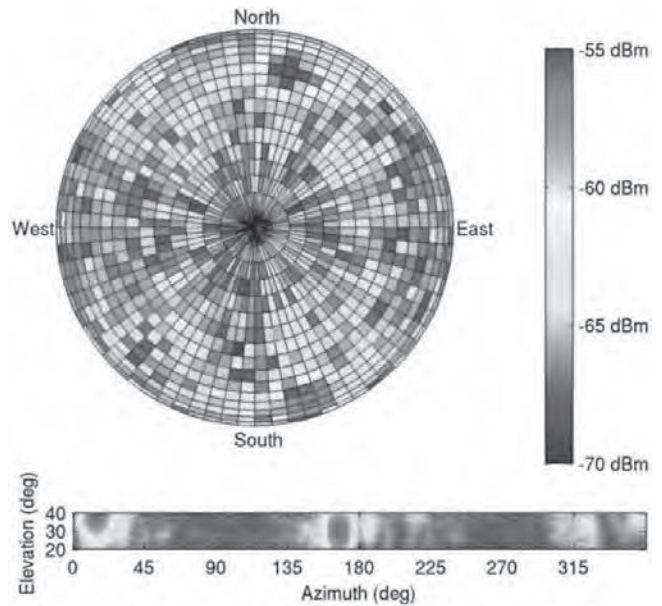
Fig. 5. Power levels of the afristar satellite in a full sky u-v plot and in an azimuth-elevation subsection

tangular North-South grid, we expect afristar also to be observed in a grating lobe when the array is pointed at 15° azimuth. The beamwidth for the 1 meter tile can be calculated width $\theta_{HP} = \theta_0/\cos(\theta)$, where θ_{HP} is the half power beamwidth and θ_0 is equal to 17° at 1480MHz for this aperture. The resulting beamwidth of 23° can be seen in the measurement. A demonstration of the capabilities of detecting an astronomical source is given with the detection of the power spectrum of the sun, plotted in fig. 6. With an on off measurement, a clear detection of the (very) strong signal of the sun is measured with the digital auto correlator back-end.

Conclusion

The first celestial observations including the sun are presented of a proto-type phased array system intended to demonstrate the potential of this concept for application in the Square Kilometer Array. These are the first results of a full scale phased array designed for radio astronomy.

Fig. 6. On-Off power spectrum measurement of the sun
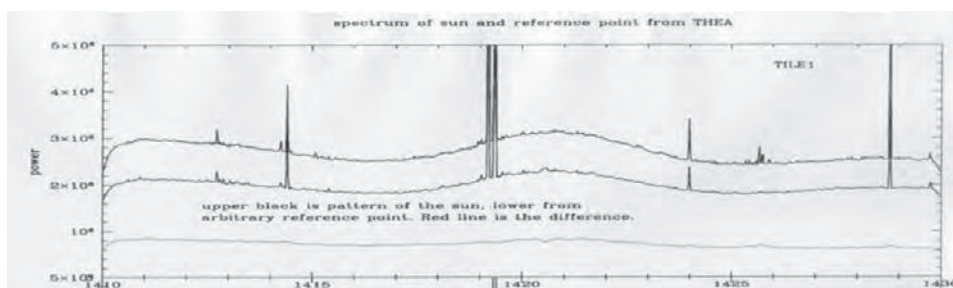
References

[1] A. B. Smolders and G.W. Kant , "Thousand Element Array (THEA)", *IEEE Int. Conf. on Antennas and Propagatio*n, Toronto, Canada, July 2000

[2] A. van Ardenne, A. B. Smolders, and G. A. Hampson, "Active adaptive antennas for Radio Astronomy; results for the R&D program towards the Square Kilometre Array", *SPIE conferenc*e, Munich, Germany, March 2000

[3] A. B. Smolders, J G Bij de Vaate, G. W. Kant, A. van Ardenne, D. Schaubert and T. H. Chio, "Dual-beam Wide-band Beamformer with Integrated Antenna Arra*y", IEEE Millennium Conference on Antenna & Propagatio*n, Davos, Switzerland, April 2000

[4] G.A. Hampson and A. B. Smolders, "A Fast and Accurate Scheme for Calibration of Active Phased-Array Antennas", *IEEE Int. Conf. on Antennas and Propagatio*n, Orlando, USA, pp 1040-1043, July 1999

[5] G. A. Hampson and J. G. Bij de Vaate, "Verification of THEA Tile Calibration and Beamforming Results using a Near Field Scanner", *IEEE European Microwave Conferenc*e, London, UK, Vol. 3 pp 141-144, Sept. 2001

[6] C. Craeye, M. J. Arts and J. D. Bregman, "Truncation Effects in Tapered-slot Antenna Arrays for Radio Astronomy Applications", *URSI 200*2, Maastricht, The Netherlands, Aug. 2002

Ledenmutaties NERG

Nieuwe leden:

Haartsen, prof. dr. ir.
 J.C., Bruchterweg 81,
  7772 BG HARDENBERG
Salm, S.A.M. van der,
 Jan Hendrik Meijerstraat 16,
  1214 NJ HILVERSUM

Nieuwe adressen:

Dijk, ir. J. ,
 Molsekiezel 253,
 3920 LOMMEL, Belgium
Goot, ir. M.R. van der ,
 Pastoor Starmansstraat 13,
  6245 MJ EIJSDEN

Kolk, ing. W.W.G.H. van de ,
 Ferdinant Bolhage 1,
 3437 NG NIEUWEGEIN
Kopmeiners, ir. R.J. ,
 Zeehondstraat 2,
 7559 BL HENGELO
Lange, ir. M.K. de ,
 Gouverneurkade 1,
 2274 KH VOORBURG
Lek, ir. I.J.H. ,
 Westvest 223,
 2611 BZ DELFT
Prasad, prof.dr. R. ,
 NTT DoCoMo Comm. Labs.
 Europe Gmbh,
 Landsberger Strasse 312,
  D-80687 MUNICH,
 Germany

Smit, ir. M.K. ,
 Weegbree 29,
 5684 JE BEST
Vrolijk, ir. M.C. ,
 Paltzerweg 238,
 3734 CT DEN DOLDER
Zanten, ir. A.T. van ,
 Goezeputstraat 25,
 8000 BRUGGE, Belgium

Multi-terabit routing in the LOFAR signal and data transport networks

Jaap D. Bregman , Gideon W. Kant, Haitao Ou
ASTRON, Oude Hoogeveensedijk 4, 7991 PD, Dwingeloo, The Netherlands
Email: {bregman, kant, haitao}@astron.nl

Abstract

The LOFAR telescope is being developed as a giant data processing machine for astronomy. An assessment is presented of photonic technologies that will enable LOFAR to be materialized in the timeframe after 2004 and we discuss the basic cost trade-offs in photonic signal transport. A summary of the LOFAR configuration and architecture is given that provides the proper input for the cost equation and leads to the definition of a short and a long-range network. For interfacing the antenna clusters as well as the processing nodes to the network we propose ten Gigabit Ethernet routing technology being developed for the PC server market.

Introduction

The digitised signals from over ten thousand antennas are combined to produce data for astronomical images, which requires an aggregated data transport bandwidth of order twenty Terabits per second in the LOFAR system [1]. There are two kinds of signal transport networks each providing half of the capacity, one for the remote antenna stations and another for all the antennas within about ten kilometre from the central processing system. The long-range network will be build based on next generation wavelength division multiplex (WDM) or optical time division multiplex (OTDM) telecom technologies, which are investigated in the Retina project [2]. An assessment study shows that the short-range network could be realized in Ten Gigabit Ethernet transport (10GbE) technology being developed for the PC server market and becoming commercially available in the coming few years. In the paper we discuss potential implementation options and use numbers with the proper order of magnitude that adhere to the basic characteristics of LOFAR as presented in the archi-

tectural design document [3]. An important aspect to be discussed is the routing configuration that interconnects order two thousand receive cluster nodes and order five hundred processing nodes to the array signal network through 10GbE ports. At the central processing facility we have a data network that interconnects order two thousand processing nodes that perform the array cross-correlation between the station beams or performs a multi beam forming operation that images the full sky. The latter operation requires twelve Terabit per second routing capacity from receive clusters to processing nodes for which a butterfly configuration of multi port router devices is proposed.

LOFAR configuration

LOFAR is an aperture synthesis array with over hundred antenna stations, each with order hundred dual polarization receptors. The stations have an exponentially increasing distance from the centre and follow curved arms that extend over 200 km. About a quarter of the stations have more or less random positions within a circle of 1 km radius leaving fifteen stations on each of the five arms. In Fig. 1 the station distribution along one such arm is indicated. So half of all stations are within 6 km of the centre and the last increment is about 60 km. We assume a central data processing facility within 3 km of the array centre.

Photonic assessment

State-of-the-art digital signal transport uses multiple 3 Gb/s electrical serial links over transmission lines and 10 Gb/s serial links over optical wave-guides. Conversion chips from low speed parallel data into high-speed serial format are priced in the tens of Euro range and allow cost effective replacement of heavy parallel connectors

Fig. 1. *Increment in km between 15 stations (|) along an exponential spiral arm (not to scale).*

| .4 | .6 | .8 | 1.2 | 2 | 3 | 4 | 5 | 8 | 10 | 15 | 20 | 30 | 40 | 60 | |

and cables by serial ones. Electrical serial cables, although more expensive than fibre optical ones, are cost effective at short distance (ten metre) when the price difference between electronic (tens of Euro) and optical (hundreds of Euro) transmission line drivers and receivers is taken into account. Once in the optical domain, cable attenuation is so low that distances op to tens of kilometres can be bridged without further equipment. A bare fibre price of 0.1 €/m then indicates that a few kilometres can be bridged before fibre cost starts dominating the total link cost.

Adding a photonic transceiver only doubles the price of a Gigabit Ethernet over twisted pair interface card used to interconnect PC type servers in a network. In 2002 all the key components to build 10GbE interface cards are commercially available, and we expect complete products by the time LOFAR equipment needs to be installed at prices that are then only a few times the current price of 1000BASE-SX Gigabit Ethernet over fibre equipment. Even router chips with over hundred I/O channels and a throughput of 0.5 Tb/s are available for a few thousand Euros, which indicates that the cost of router boxes will be dominated by the data interfaces. The PC server based network applications organized in Wide and Metropolitan Area Networks are expected to use 10GbE technology and constitutes a market big enough to warrant PC level prices for this high speed data communication.

Network cost equation

The total cost of a connection between a LOFAR station and the central processing facility includes the cost of trenching, the number of fibres in a trench and the photonic transceiver. We neglect the cost of pre-processing to reduce the data rate. In designing a system we combine technologies that have different marginal cost effects when the system is rescaled in a certain parameter. For a data transport network the performance issues are distance and bandwidth. An optimum choice is found when all three cost contributions are about equal. Fibre and transceiver cost are matched at an average fibre length of three kilometres. For a trunk arm with an exponentially increasing distance between the branching points we then find a maximum distance of about six kilometres from the centre to provide an average fibre length of three kilometres. Then half of all receptors could be connected to the central processing centre. Transpor-

ting the full potential bandwidth requires one fibre at 10 Gb/s for every five dual polarization receptors, which leads to a total of thousand fibres with an average length of 4.5 km to the processing centre. The five arms then need thirty kilometres of trenching, which means an average of hundred and fifty fibre pairs in a trench. Typical trenching cost is tens of Euros per metre and just equals the fibre cost. Having made these initial choices the cost of trenching is a third of the total cost. The average trench length for the fifty stations of the inner array is now 0.6 km per station and we can express the average station connection cost as just two kilometres trench equivalent. The marginal cost of adding one more station on an arm is dominated by the trenching cost, the so-called last mile problem. However connecting the next two stations on each arm requires just over three kilometres per station and does not yet increase the average cost.

We have shown that full 200 Gb/s data transport from the centre 60 % of the stations out till thirteen kilometres from the centre is a system optimum where the cost of trenching, fibres and transceiver is balanced.

Connecting the more remote stations by exponentially extending the trench along the arms drives up the average connection cost. This means that we have to look into alternative solutions that share the dominating trenching cost with other users. The most attractive route is leasing dark fibre from external parties and use own equipment. The fibre and shared trench cost for these remote stations dominates over the cost of the 10GbE transceiver boards, and it becomes cost effective to use WDM or OTDM technology to transmit 40, 80 or 160 Gb/s from each remote station instead of only 10 Gb/s on a single fibre.

This shows that the remote stations can operate at 10 Gb/s in the initial phase of the project requiring forms of data compression and reduction at the remote stations. When the advanced data transport technology becomes available in a later phase, it could be installed together with additional processing hardware to support the enhanced bandwidth of the system.

LOFAR architecture

LOFAR is a giant data processing machine where signal data from a few thousand receive clusters are pre-processed and transported to a central faci-

lity for further processing. A basic logical block is the receive cluster where the signals of about five dual polarization receptors are digitised and buffered before asynchronous transport to the processing nodes where the beam forming operation is executed. Further architectural elements are routing devices, fibre optical cabling network, optical repeaters and fibre optical multiplex units. It is attractive to use a single type of data interface for all this equipment and 10GbE is proposed as being well matched to commercial off-the-shelf equipment in the 2005 time frame. The central facility is a cluster of a few thousand PC servers interconnected with a high bandwidth network that transports the signals between all the processing nodes.

Three processing operations are performed on the antenna signals. First the wide band signal of each antenna is divided in a number of sub bands. The second operation is beam forming, where the signals of a group of clusters that constitute a station are combined for each sub band into a beam that selects a certain part of the sky. Finally the beam of each station is cross-correlated against the beam of all other stations. The second and third class of operations require each about thousand processing nodes. Therefore, frequency or time slicing needs to be done on the receptor data streams such that the slices are routed to different processing nodes. Then the data slices from different receptors are merged for further combined processing in a co-processor board that provides the computational muscle to each PC server node.

In the initial phase of the LOFAR project only a single beam is formed from each receptor bandwidth slice and the first step in hierarchical beam forming could be executed at the receive cluster level, which reduces the effective output data rate by a factor five. Then five receive clusters and a set of beam forming processing nodes could be daisy chained by 10GbE links. With a proper forwarding process in each node a ring router is formed. One of the processing nodes is connected to a second ring, which combines the cluster set outputs and that also includes one or more nodes of the central processor. This set of beam forming processing nodes could be co-located at the central processing facility, or located at an individual station and then reduce the capacity requirement for the long-range network. The central processing cluster network could be organized as a three-dimensional torus [4] that supports an average inter node transport capacity of order Gb/s, which is adequate to support the cross correlation functionality. This situation is depicted in Fig.2, where 10GbE fibre optic links are used for each receive cluster of the inner array. The stations of the outer array have a single fibre optic link, requiring additional transceivers as repeaters for the remotest stations [5].

Instead of forming a limited set of beams in a hierarchical fashion for each station and cross correlating them, an all sky imaging mode could be provided that uses only the cluster signals of the inner array, together with the processing power available in all the nodes. However this beam for-

Fig. 2. Network architecture for the first phase of LOFAR based on 10GbE technology and ring routing.
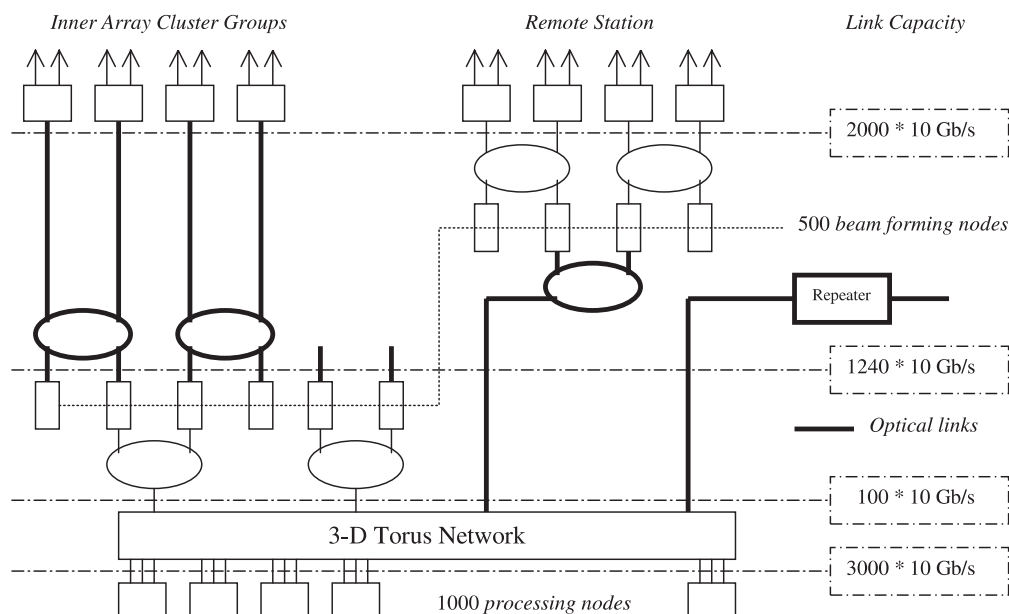
ming operation would require twelve Tb/s throughput from the receive clusters to the two thousand processing nodes. This could be realized by replacing the three dimensional torus by a butterfly configuration of multi-port router devices, still using the same 10GbE interface cards. A final step is enhancement of the long-range network to support full sky imaging also by the remote stations. This could be realized in WDM / OTDM technology where many 10 Gb/s streams are multiplexed on a single fibre. This situation is visualized in Fig. 3.

Conclusions

A network based on 10GbE transceiver and routing technology being developed for the emerging ten Gigabit Ethernet market is a viable option for LOFAR. We have shown that full 200 Gb/s data transport for 60 % of the stations out till 13 km from the centre is a system optimum after 2004 when the cost of trenching, fibres and transceivers is balanced. This gives complete freedom in locating hierarchical beam forming near the receive clusters or at the central processor.

The remote stations could operate at 10 Gb/s in the initial phase of the project requiring forms of data compression and reduction like local beam forming. When advanced WDM / OTDM data transport technology becomes available by 2007, it could be installed together with other planned processing hardware upgrades of the system and eliminates the need for station level beam forming. We postpone our most demanding applications till advancing technology provides high bandwidth processing according to Moore's law at the appropriate marginal system enhancement cost.

A network routing approach is proposed that allows all processing nodes in the network to be accessed efficiently by all receive clusters. This provides for dynamic reconfiguration of the processing constellation to meet observation requirements. A key feature is the bandwidth scalability, which allows network configurations to be simulated and evaluated using current one Gigabit Ethernet technology.

References

[1] J.D. Bregman, "Concept Design for a Low Frequency Array," SPIE proceedings Volume 4015, March 2000

[2] J. Verhoosel, M. de Vos, E. J. van Veldhuizen, T. Koonen, H. de Waard, "A multi-terabit optical fibre network for a LOFAR telescope," Proceedings URSI GA, July 2002, ibid.

[3] K. v.d. Schaaf, "LOFAR Architectural Design Document," LOFAR-ASTRON-ADD-006, www.lofar.org

[4] C.M. de Vos, K. v.d. Schaaf , J.D. Bregman, "Cluster computers and Grid Processing in the first Radio Telescope of a New Generation," *Proceedings of the First IEEE/ACM International Symposium on Cluster Computing and the Gri*d, Brisbane, May 2001, pp. 156-160

[5] H. Ou, M. v. Veelen, D. Kant, "Assessment of gigabit Ethernet technology for the LOFAR multi-terabit network," Proceedings URSI GA, July 2002, ibid

Fig. 3. Network architecture for the second phase of LOFAR including WDM/OTDM technology.

Inner Array Cluster Groups

Remote Station

Link Capacity

2000 * 10 Gb/s

1200 * 10 Gb/s

WDM

40 * 200 Gb/s

WDM

2000 * 10 Gb/s

2000 * 10 Gb/s

2000 * 10 Gb/s

2000 *processing nodes*
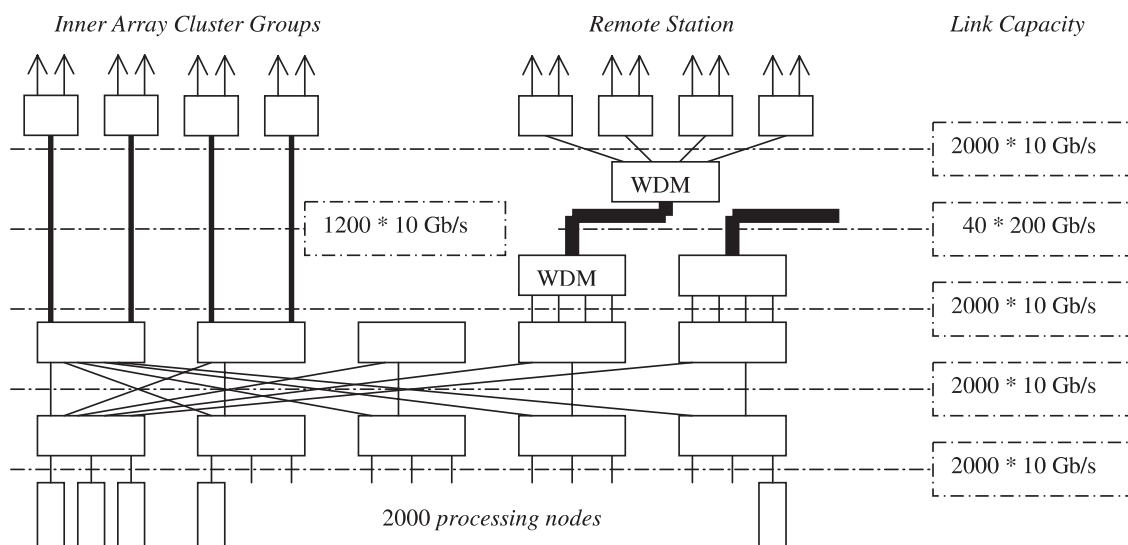
Photonic Bandgap Antennas and components for Microwave and (Sub)millimetre wave Applications

Peter de Maagt*, Belen Arredondo Conchillo*, Luca Minelli*, Iñigo Ederra**, Ramón Gonzalo**, and Andrew Reynolds***

*Electromagnetics Division, European Space Research and Technology Centre, ESTEC, PO Box 299, 2201 AG Noordwijk, The Netherlands.

* * Electrical and Electronic Engineering Department, Universidad Pública de Navarra,Campus Arrosadia, E-31006, Pamplona, Navarra, Spain

***now with Nortel Networks UK Limited,Harlow Laboratories, London Road, Harlow, Essex, CM17 9NA, United Kingdom

Abstract

This paper discusses some application areas of PBG technology and shows some results of realised antennas and PBG waveguides at microwave and (sub)millimetre wave frequencies. The results are drawn from work on using 2-D PBG crystals as substrates for both single patch and patch array antennas at microwave frequencies and 3-D PBG crystals at submillimeter wave frequencies. In order to get the most of this technology, a fully integrated receiver should be developed in which not only the antennas but also all the other components were designed using PBG technology. Some emphasis is placed on PBG waveguiding. This paper also contributes to the ongoing discussion within the PBG community by briefly mentioning the limiting conditions of the coupled cavity waveguiding mechanism

Introduction

Periodic electromagnetic materials are presently one of the most rapidly advancing sectors in the electromagnetic arena. Periodic structures such as photonic bandgap crystals allow us to engineer control over the propagation of electromagnetic waves to an extent that was previously not possible. Consequently they have been studied energetically in recent years and the literature reflects the fact that the initial academic studies have now matured. Emphasis is now being placed on finding tangible applications combined with detailed modelling.

Owing to the tremendous potential of photonic bandgap (PBG) structures there is a plethora of applications in which these can be used. Communications services are one example of an area that is becoming increasingly important. There has been a significant increase in demand for high-speed data services for voice and multimedia applications, particularly for accessing the Internet and the fixed and mobile services. As a result, broadband microwave wireless access has emerged. Technically, these applications look for new frequency spectrums with higher operational frequencies around 30 GHz, 40 GHz and 60 GHz for point to point, point-to-multipoint and high density fixed services, respectively.

Furthermore, technology in the sub-mm wave region of the electromagnetic spectrum is currently experiencing an explosive growth. The growth is fuelled in part by the need for faster signal processing and communications, high-resolution spectroscopy, atmospheric and astrophysical remote sensing and medical imaging against cancer. The increased atmospheric absorption and specific molecular resonances observed over this range of frequencies gives rise to applications in secure ultra-high bandwidth communication networks.

Novel PBG components and subsystems offer a very promising alternative to overcome the limitations of the current technology (ohmic losses, bandwidth, gain, efficiency). PBG technology can represent a major breakthrough with respect to the current planar approaches, mainly due to their ability to guide and control efficiently electromagnetic waves. In order to get the most of this technology, a fully integrated receiver or emitter system should be developed in which all the components were

designed using PBG technology. The first step in order to achieve this goal is the design of the individual components.

This paper discusses the applications areas and shows some results of realised antennas and PBG components at microwave and (sub)millimetre wave frequencies.

Combined research and prototyping at the conventional microwave and the more challenging sub-mm frequency range has guaranteed a broader aptitude, applicability and feasibility of the developed modelling and testing facilities. It ensures an attractive synergy between the applications driven developments at microwave devices, with the technologically more demanding development of sub-mm wave systems. It also simultaneously provides verification of scalability in design and provides essential insight into any possible optical applications of such devices.

Microwave antennas

A multitude of down to earth PBG applications exist especially within the microwave and low millimetre-wave region. Electronically scanned phased arrays find their use in many applications. For example constellations of satellites can be used for high data-rate transmission for multi-media applications. These applications require scanned multi-beam antennas with relatively wide bandwidth. Each beam is usually working in dual circular polarization. Most of these constellations will work at frequencies up to 30 GHz. The use of active phased array made in microstrip technology is

then an attractive solution. However the need for bandwidth and scanning increases the risks caused by surface waves. A very promising way to eradicate the problems created by surface waves, e.g. scan blindness, while at the same time improving performance, is to use a photonic bandgap crystal instead of standard dielectric substrates.

The measured near field pattern [1] of two identical patch antennas that have been placed in an E-Plane array configuration is shown in figure 1.

PBG substrates also provide benefits for single microstrip patch antennas. Such patch antenna designs can have limitations, restricted bandwidth of operation, low gain and a decrease in radiation efficiency due to surface wave loss. While thickening the substrate thickness increases the operational bandwidth, a trade off must be made with the increased excitation of substrate modes. The utilization of a photonic crystal substrate in place of the original bulk substrate has shown to improve the antenna radiation efficiency and reduce the side lobe level [2].

Another microwave application is high precision GPS. High precision GPS surveying can make measurements with sub-centimetre accuracy levels. While software can greatly reduce multipath errors, extra precautions that can shield the antenna from unwanted multipath signals are needed to obtain these accuracies. Choke rings provide excellent electrical performance for GPS antennas, but they are usually very large, heavy and costly. Making use of the fact that Metallo-Di-

Figure 1: Measured near field pattern. The red rectangles in the right plots are the scanned area. The top and bottom rows correspond to the conventional and the PC substrates. The left and right columns are at 17 GHz (inside the gap) and 14.5 GHz (outside the gap) respectively. Each plot is normalised to its maximum value.
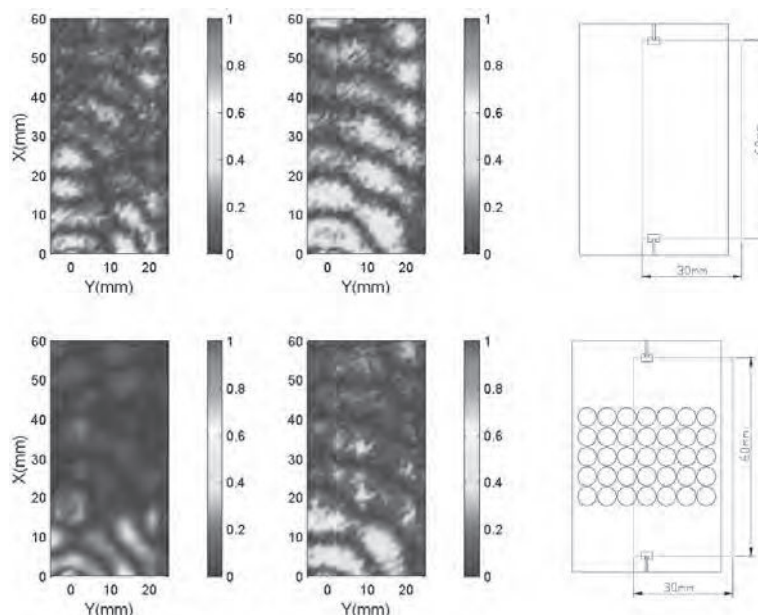
electric PBG antennas can behave as Artificial Magnetic Conductors, one can design PBG solutions in printed circuit technology [3]. Also, this technology may prove useful in mobile antenna handset designs and enable the radiation (Specific Absorption Rate, SAR) into the operator's hand and head to be reduced. Note that soon all mobile phones will display the SAR value of the handset.

(Sub) Millimeter wave antennas

A new generation of scientific space borne instruments, included in both Earth observation and scientific missions, is under consideration at millimetre and sub-millimetre wavelengths. As the frequency increases, a planar structure that integrates the antenna, mixer, local oscillator and all peripheral circuitry onto one single substrate becomes an attractive option. While conceptually simple, in practice it is challenging to develop and test an integrated planar antenna on a semiconductor substrate that has good radiation efficiency and can be easily integrated with the active circuit. One of the problems encountered, is that planar antennas on high dielectric constant substrates couple a significant fraction of the input power into substrate modes. Since these do not contribute to the primary radiation pattern, substrate mode coupling is generally considered as a loss mechanism. By removing the possible existence of substrate modes by using a PBG substrate the problem can be overcome, exemplifying the application of PBG materials. The radiation pattern of an integrated antenna system at 500 GHz [4] is shown in figure 2. The PBG crystal used is the so-called layer-by-layer or woodpile structure [5].

PBG waveguiding

An ideal PBG crystal is constructed by the infinite repetition of identical structural units in space. Considerable effort in theoretical, experimental and material fabrication research has predicted and demonstrated many of the properties of these ideal crystals. Introducing some disorder by placing a "defect unit" within an otherwise perfect PBG crystal can create localised transmission peaks within the forbidden band gap of the structure. Previous work has suggested PBG crystal channel waveguides that consist of a line defect introduced into an otherwise perfect 2-dimensional crystal. Various bends, couplers and add-drop multiplexers have also been proposed [6,7]. An example of PBG waveguide is shown in Fig. 3. The PBG structure was formed by air holes in a dielectric substrate ($\varepsilon_r = 10.2$) with metal plates at the top and bottom (see Fig. 3). A microstrip line was used to excite the PBG waveguide needing a transition between the PBG waveguide width and the 50 Ω microstrip line. Measurement transmission results of a conventional microstrip waveguide including the aforementioned transition and a PBG waveguide are presented in Fig. 3. The microstrip waveguide was fabricated in order to extract information about the losses coming from the connector-microstrip transition and the effect of the stationary wave originated between connectors. In the PBG case, the transmission results show a reflection peak at 13 GHz which coincides with the Distributed Bragg Reflection (DBR) effect. Apart from this, the PBG transmission curve shows equivalent losses as the conventional waveguide demonstrating that the PBG waveguide is a valid alternative to guide the power at millimetre wave frequencies.

Figure 2: 500 GHz dipole antenna on top of woodpile a) Electron Microscope photograph, b) Measured Radiation pattern for the E- and H-planes (Black line E-plane, Red Line H-plane).
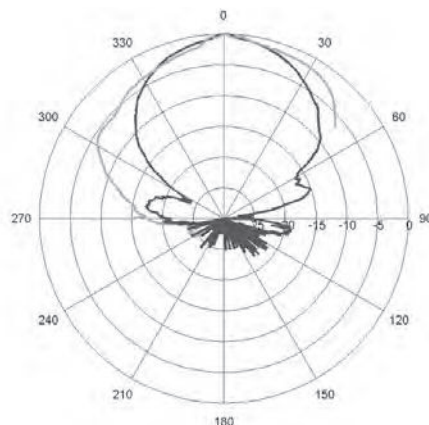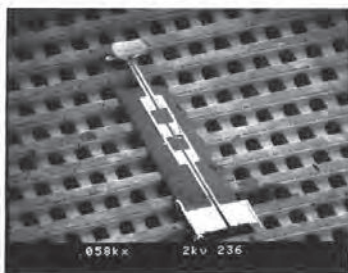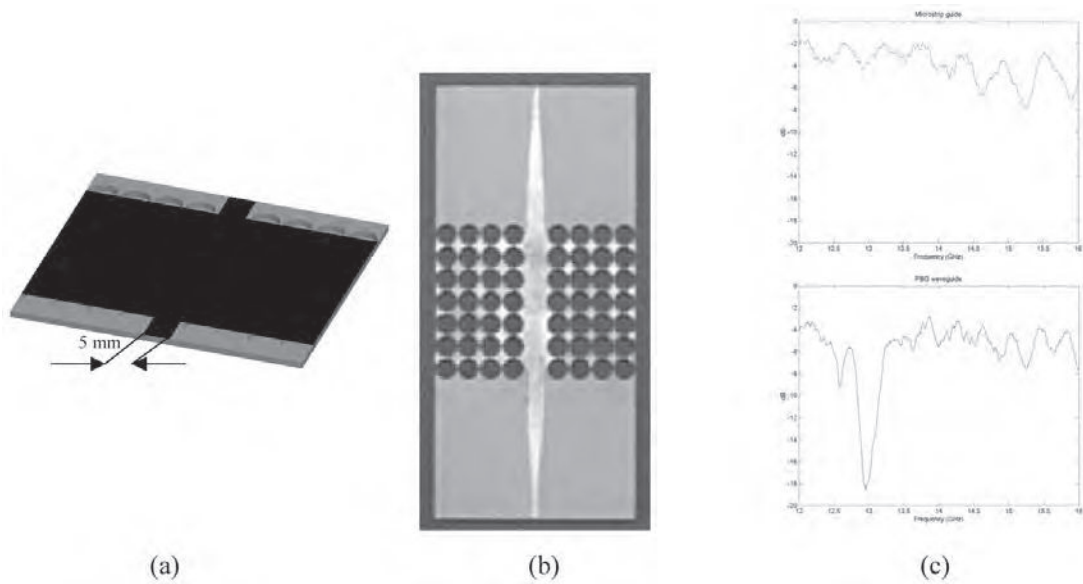
Figure 3: PBG waveguide based on a linear defect (a) PBG waveguide between metal plates. (b) The inner section of the fabricated PBG waveguide, (c) Transmission measurements of conventional microstrip waveguide (top) and PBG waveguide (bottom)

Recently an alternative to the linear defect waveguide has attracted considerable attention. This alternative makes use of a periodic chain of localised defects that have been either completely or partially in-filled. The introduction of several localised defects, within coupling distance of each other, opens up a mini-band of allowed transmission [8,9]. Chains or cascades of localised defects form a mechanism for waveguiding, commonly referred to as coupled cavity waveguides, CCW.

Experimental verification of 2-dimensional CCW's has been performed in the microwave regime. It has frequently been assumed that bends can be introduced into the waveguide path by taking advantage of the crystal's inherent lattice symmetry without consequential bend reflection loss. However, it can theoretically be shown that the mini pass band created by coupled cavity waveguide bends may only reach 100% transmission for a strict set of criteria [9]. Figure 4 shows some

Figure 4: Spectral response of a bend in a defect chain in a hexagonal PC lattice; a) Image of a bend in a 1-in-2 defect chain, b) reflection for varying ratio of the next nearest (c1) to nearest neighbour (c0) interaction.

(a)

(b)
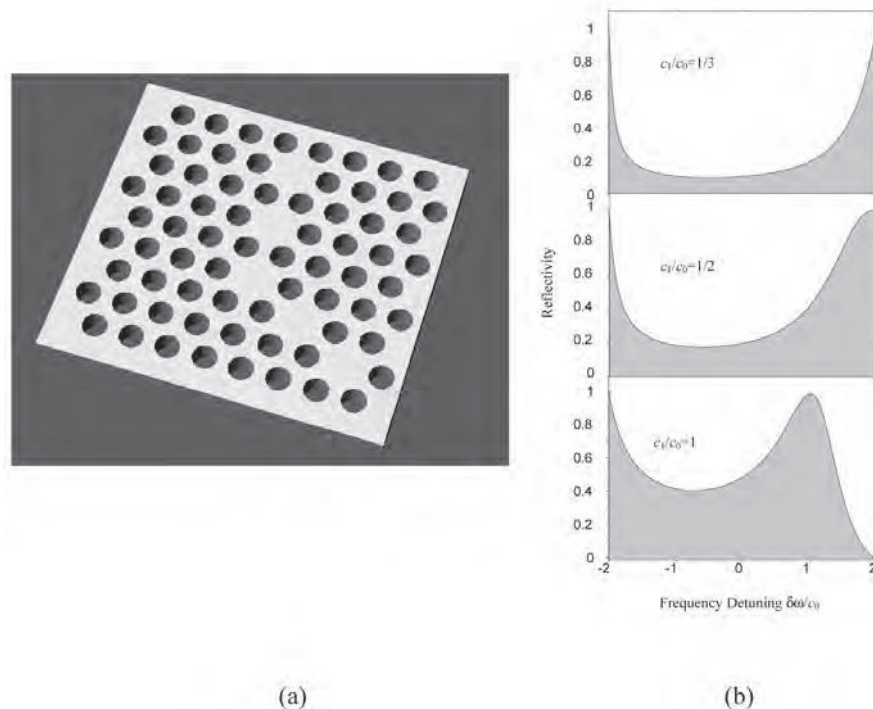
reflections losses that might occur for a CCW-bend in a hexagonal lattice.

Conclusion

Currently, there is a need for wide band device functionality, and ideally multifunctional devices. At millimetre wave frequencies, the existence of components for such systems is currently very limited. As long as the market demands these broadband communications, the development of novel communication components and subsystems for mobile equipment and base stations will always be in demand. Ideally, these components and sub-systems would be required to be dynamic, re-configurable and multifunctional.

The technological potential of electromagnetic crystals for developing such novel components and subsystems offers a very promising alternative to overcome the limitations of the current technology. PBG technology represents a major breakthrough with respect to the current planar approaches, mainly due to their ability to guide and control efficiently electromagnetic waves.

In order to drive this technology towards the market place we will need to identify component(s) feature(s) of photonic bandgap structures that give added value over and above current approaches. In this paper some examples have been presented.

References

[1] R. Gonzalo, G. Nagore, I. Ederra, B. Martinez, H. Pellemans, P. Haring Bolivar, and P. de Maagt, *"Coupling between patch antennas on photonic crystals"*, Proc. 24th ESTEC Antenna Workshop on Innovative Periodic Antennas: Photonic Bandgap, Fractal and Frequency Selective Structures, 30 May-1 June 2001, Noordwijk, the Netherlands, pp.17-22.

[2] R. Gonzalo, P. de Maagt, and M. Sorolla, *"Enhanced patch antenna performance by suppressing surface waves using Photonic Band-Gap struc-tures"*, IEEE Transactions on Microwave Theory and Techniques, Vol. 47, No. 11, pp. 2131-2138, November 1999.

[3] L. Minelli, Study of Metallo-Dielectric Photonic Bandgap (MDPBG) structures, ESTEC report 2002.

[4] R. Gonzalo, I. Ederra, C. Mann, and P. de Maagt, *"Radiation properties of terahertz dipole antenna mounted on photonic crystal"*, Electronics Letters , Vol. 37, Iss.10, 10 May 2001, pp. 613 –614.

[5] R. Gonzalo, B. Martinez, C. Mann, H. Pellemans, P. Haring Bolivar and P. de Maagt , *"A Low Cost Fabrication Technique for symmetrical and asymmetrical Layer-by-Layer Photonic Crystals at Sub-Millimetre Wave Frequencies"*, accepted for publication in IEEE Transactions on Microwave Theory and Techniques, October 2002.

[6] S. Fan, P. R. Villeneuve, J. D. Joannopoulos and H. A. Hauss, *"Channel Drop Filters in Photonic Crystals"*, Optical Express, Vol. 3, Nº 1, pp. 4-11, April 1998.

[7] A. Mekis, J. C. Chen, I. Kurland, S. Fan, P. R. Villeneuve and J. D. Joannopoulos, *"High Transmission through Sharp bends in Photonic Crystal Waveguides"*, Phys. Rev. Lett., Vol. 77, No 18, pp. 3787-3790, October 1996.

[8] A. Reynolds, U. Peschel, F. Lederer, P. Roberts, T. Kraus and P. de Maagt, *"Coupled defects in photonic crystals"*, IEEE Trans. on Micr.Theory and Techn , vol. 49 nr. 10 , October 2001, pp. 1860-1867.

[9] U. Peschel, A. Reynolds, B. Arredondo, F. Lederer, P. Roberts, T. Krauss, P. de Maagt, *"Transmission and Reflection Analysis of Functional Coupled Cavity Components"*, IEEE Journal of Quantum Electronics, accepted for publications in the special issue: Photonic Crystal Structures and Applications, June 2002.

Josephson arbitrary waveform synthesizer: electronics for a quantum standard for ac voltage

H.E. van den Brom, E. Houtzager, G. de Jong and O.A Chevtchenko
NMi Van Swinden Laboratorium, P.O. Box 654,
2600 AR Delft, The Netherlands, HvdBrom@NMi.nl

Abstract

A new primary standard for AC voltage based on pulse driven Josephson junction arrays is under development. In this paper, preliminary spectral measurements and simulations are presented on a fast switching multiplexer unit built for the high precision synthesis of arbitrary waves. First order delta-sigma modulation is used to represent the wave to be synthesized. The first results are promising with respect to the conditions for high precision filtering of the quantization noise, i.e. a high signal-to-noise ratio is expected for the demodulated signal.

Introduction

Research in the field of electrical metrology mainly focuses on the development of so-called quantum standards. The main goal is to realize electrical quantities by means of laws of nature instead of "artifacts". A nice example is the primary standard of resistance: the Ohm can be related to the quantum Hall effect instead of a physical high quality resistor. The latter can be drifting in time, which is difficult to verify, or it might change its value when treated not too carefully. Relating standards to quantum mechanical phenomena in principle drastically decreases the uncertainty and makes them much more reliable.

The most familiar quantum standard is the DC Josephson array voltage standard. For two superconductors separated by a very thin insolating layer (a so-called Josephson junction), a DC voltage difference will occur when an RF bias current is supplied. The voltage V will only depend on the frequency f of the supplied signal and on constants of nature:

$$V = n \frac{2e}{h} f \qquad (1)$$

where n is a tunable integer number that can be tuned using for example a DC bias current, e is the electron charge and h is Planck's constant. This voltage is known within a relative uncertainty of 10^{-9}, since frequency can be determined very accurately (relative uncertainty better than 10^{-14}).

In the last years research has been started to develop a quantum standard for AC voltage based on the Josephson effect [1-5]. The first problem was the hysteresis in the current-voltage (*I*-V) characteristics. Without special precautions, the response of an ordinary superconductor-insulator-superconductor (SIS) Josephson array to a DC bias is unpredictable, i.e. it is not possible to control the output of the array by simply varying the bias current. However, intrinsically shunted Josephson arrays, such as a superconductor-insulator-normal-insulator-superconductor (SINIS) array [6], show non-hysteretic *I*-*V* characteristics. This makes them suitable for the development of a programmable voltage standard.

One possibility to program the array is to divide it into binary sections [1,2,5] that can be biased with independent DC current sources. By activating a specific number of binary sections, an arbitrary DC voltage can be generated. By rapidly switching between the binary segments, the voltage can be changed in time, such that an AC voltage occurs. The main concern in using this technique is to overcome problems rising from fast switching events.

The second possibility is to modulate the drive frequency using a digital code [3,5]. A controlled train of pulses replaces the RF sine wave, consisting of a continuous series of pulses. Each individual pulse "excites" the Josephson array. When this train of pulses contains a delta-sigma modulated code for
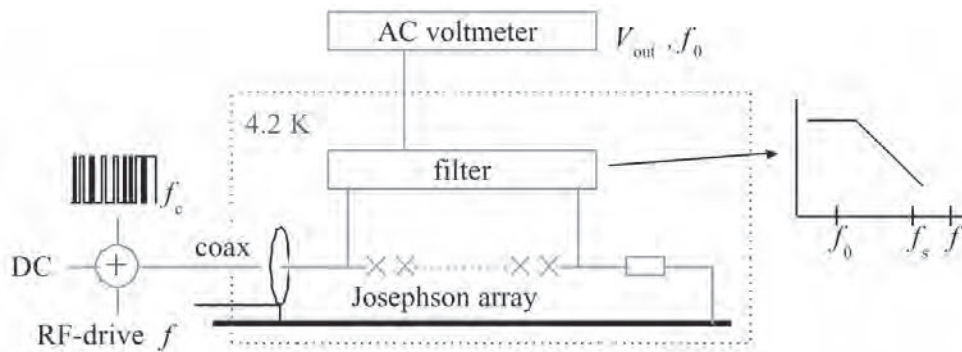
Fig.1: Schematic overview of the future pulse drive set-up. Digital code, DC offset and RF signal will be combined and fed to a Josephson array. The synthesized voltage has to be filter in order to recover the original signal.

an arbitrary wave, after filtering the output of the Josephson array a signal of calculable arbitrary waveform will arise, see Fig.1. This Josephson arbitrary waveform synthesizer will be the basis of a new AC Josephson array voltage standard [8], which is the topic of this paper.

Driving the Josephson array

The conventional way of driving a Josephson array is by applying an RF signal, which results in a quantized voltage over the array, as in (1). However, the drive mechanism of Josephson junctions is based on the fact that instead of the voltage itself it is the superconducting phase that is quantized. The AC Josephson equation directly relates the time derivative of the difference in superconducting phase, ϕ, to the voltage over the junction,

$$\frac{1}{2\pi}\frac{d\phi}{dt} = \frac{2e}{h}V \tag{2}$$

A non-linear second order differential equation relating the phase to the applied current $I(t)$ is obtained by combining (2) with the DC Josephson relation,

$$C\frac{dV}{dt} + \frac{V}{R} + I_c \sin\phi = I(t) \tag{3}$$

where C denotes the capacitance between the two superconductors, the resistance R reflects dissipation, and I_c is the maximum supercurrent the junction can support. Simulations show that the junction responds to current pulses above a certain threshold by a phase shift of 2π (or $n \cdot 2\pi$ when a current above the nth threshold is applied), just as a damped pendulum responding to an applied torque. Integrating (2) one can see that this corresponds to a quantized time integral of the voltage.

In order to change the voltage over the array, instead of a sine wave, an arbitrary sequence of pulses can be offered. However, managing a

sequence of individual pulses with a bit rate comparable to a typical RF drive frequency of 10 GHz is very difficult. Instead, one can combine an RF signal just below the threshold with a two-level signal that lifts the pulses above the threshold. This way, from a simplified perspective the array in fact switches between the $n = 1$ and the $n = -1$ plateau of the I-V curve. When the two-level signal contains the pulse code modulation of an arbitrary wave, after demodulation of the output of the Josephson array the desired arbitrary wave is recovered. Note that in this case the Josephson array only serves to regulate the amplitude of the synthesized arbitrary wave with high accuracy.

Pulse drive electronics

The pulse drive electronics forms the heart of the setup. It must provide proper switching speed, amplitude, bit pattern and synchronization. Synchronization between digital code and RF signal can be obtained only if the sinusoidal frequency, f, equals half-integral multiples of the sampling frequency, f_s. In order to avoid steeply rising edges this ratio should be 3/2, while the digital code is separated into only three pairs of consecutive bits, i.e. 00, 01 and 11, avoiding 10 (or using 10 and avoiding 01) [3]. The rise time between two successive bits should be smaller than half the period of the sine wave. The SINIS arrays are fabricated for frequencies around 10 GHz [7], which means that the rise time should not exceed 50 ps. The specification of the multiplexer fulfills this requirement; using a 4 GHz real time oscilloscope we were only able to verify the rise time to be less than 100 ps. Previous measurements and simulations were limited to the time domain [9]; in this paper we focus on the spectrum of the digital code.

The dedicated pulse drive electronics receives the data from the computer through 16 parallel lines with a bit rate of 13.33 MHz. The electronics multi-
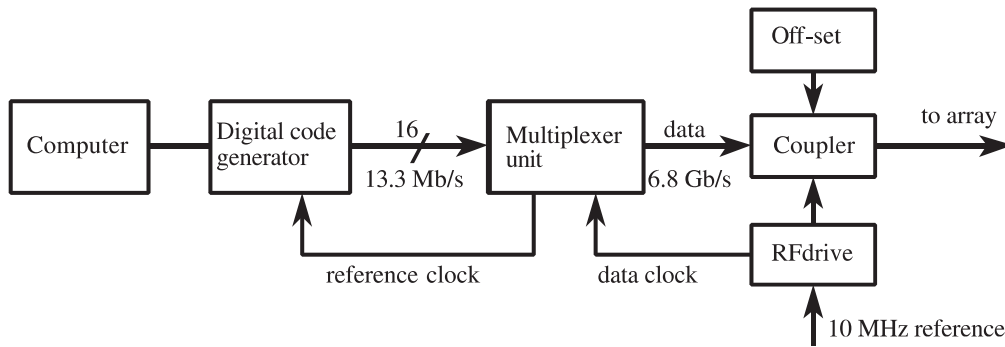
Fig.2: Schematic overview of the pulse drive electronics built for generation of the digital code.

plexes the input such that its output contains segments of 32 repetitions of pairs of two consecutive bits, i.e. the input series A0, A1, A2, …. , A7, B0, B1, ... ,B7 is converted into an output series 32*(A0,B0), 32*(A1, B1, ... 32*(A7, B7). This way the output has a bit rate of 6.83 GHz, which is two third of the RF signal frequency of 10.24 GHz. However, the actual information rate is much lower, since this kind of multiplexing does not add information.

Delta-sigma modulation

For high-resolution representation of low frequency signals delta-sigma modulation is an efficient technique. The quantization noise of this type of modulation is sinusoidal instead of constant in frequency: lower for low frequencies but increasing for higher frequencies [10]. Obviously, for such a spectrum it is easier to suppress the unwanted frequency components.

The working principle of a first order delta-sigma modulator is based on an integrator and a feedback loop. The integrator accumulates the difference between the average input and the actual output; eventually the feedback loop will correct for this difference.

In order to modulate an arbitrary wave as discussed in the previous section, avoiding steeply rising edges, first we apply a three level delta-sigma modulation. The three levels –1, 0, 1

Fig.3: Measured spectrum of a multiplexed delta-sigma modulated 10.4 kHz sine wave from DC to 1 MHz (top left), 10 MHz (top right), 100 MHz (bottom left) and 1 GHz (bottom right). The power is indicated in dB.
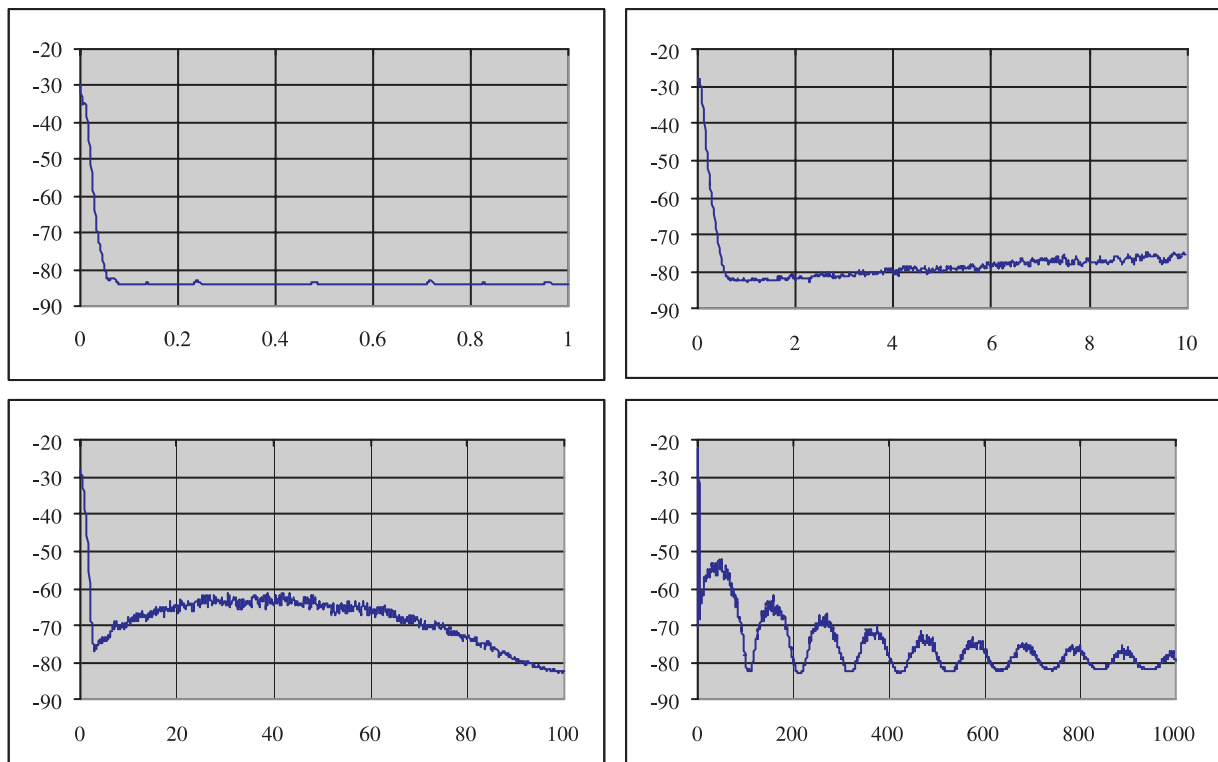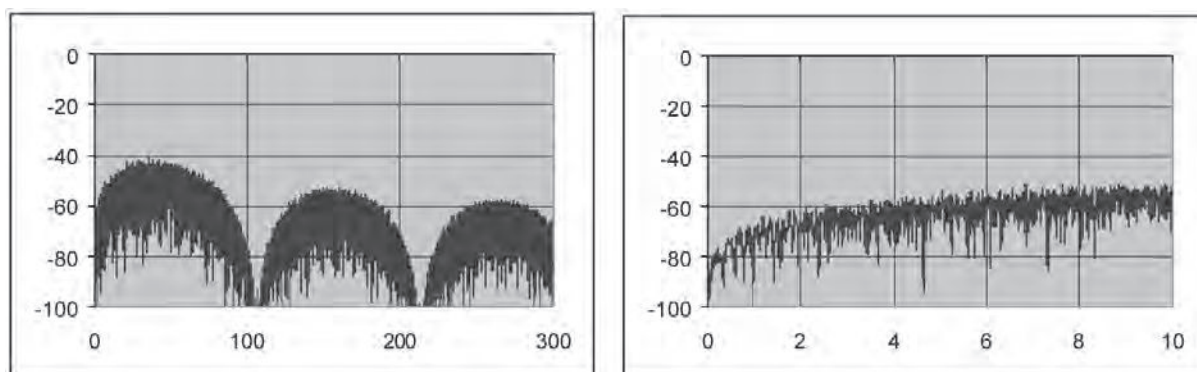
Fig.4: Simulated spectrum of a delta-sigma modulated 10.4 kHz sine wave up to 300 MHz (left) and 10 MHz (right). On the vertical axis the power is indicated in dB. The spectrum is based on a direct Fourier transform (DFT), which means that it contains no absolute amplitude information.

are then converted into the two-bit level pairs 00, 01, 11, respectively. Hence, the actual sampling rate f_s of the modulator equals eight times the update frequency of the generator, i.e. f_s = 106.7 MHz.

We performed measurements and simulations on a first order delta-sigma modulated 10.4 kHz sine wave, such that (apart from the 10.4 kHz peak) the spectrum only contains modulation noise. A 10240 digit representation of one cycle of the sine wave is constructed. The number of digits N is one-to-one related to the frequency f_0 of the signal, due to the fixed output rate of the generator: $f_0 = f_s/N$. The digital representation of the signal is three-level delta-sigma modulated and converted into a two-level digital code. This two-level code is then generated and multiplexed.

As can be seen from Fig.3 and Fig.4 respectively, experiments and simulations are in good qualitative agreement. Just above the signal band (i.e. from DC to 10.4 kHz) the quantization noise is given by the noise floor of the spectrum analyzer. The noise increases in a sinusoidal way with frequency, up to half the sampling frequency, as predicted by theory [10]. The multiplexing unit extends the usual delta-sigma spectrum from a quarter period of a single sine towards a diminishing repetitive structure. The repetition rate of this structure is the sampling frequency f_s = 106.7 MHz. Demodulation of the digital code can be performed by high precision low pass filtering. Since close to the signal band the quantization noise is at minimum, a high signal-to-noise ratio is expected.

These preliminary results show that the use of our electronics in combination with a delta-sigma modulated signal is promising. The insertion of a Josephson array will regulate the amplitude of the

arbitrary wave to be synthesized. Losses in the cables and the filters for the suppression of the quantization noise will be the main sources of uncertainty.

Conclusion

A new standard for AC voltage based on pulse driven Josephson junction arrays is under development. As a first step, preliminary spectral measurements and simulations have been presented on a fast switching multiplexer unit built for the high precision synthesis of arbitrary waves. First order delta-sigma modulation is used to represent the wave to be synthesized. The first results are promising with respect to the conditions for high precision filtering of the quantization noise. Future work will concentrate on the development of suitable low-loss filters. Finally, all parts of the set-up, including Josephson array, have to be assembled in order to perform precision measurements. The intended Josephson arbitrary waveform synthesizer (JAWS) has the potential to become the primary standard for AC voltage.

Acknowledgements

References

[1] C.A. Hamilton, C.J. Burroughs, and R.L. Kautz, "Josephson D/A converter with fundamental accuracy", IEEE Trans. Instrum. Meas. 44, 223 (1995)

[2] S.P. Benz, C.A. Hamilton, C.J. Burroughs, T.E. Harvey, and L.A. Christian, "Stable 1-volt programmable voltage standard", Appl. Phys. Lett. 71, 1866 (1997)

[3] S.P. Benz, C.A. Hamilton, C.J. Burroughs, T.E. Harvey, L.A. Christian, and J.X. Przybysz, "Pulse-Driven Josephson Digital/Analog Converter", IEEE Trans. Appl. Supercond. 8, 42 (1998)

[4] For a review, see C.A. Hamilton, "Josephson voltage standards", Rev. Sci. Instrum. 71, 3611 (2000)

[5] In the European Union a feasibility study was conducted in the frame of the ProVolt project (contract no. SMT4-CT98-2239).

[6] R. Behr, H. Schulze, F. Müller, J. Kohlmann, and J. Niemeyer, "Josephson arrays at 70 GHz for conventional and programmable voltage standards", in IEEE Trans. Instrum. Meas., Vol. 48, No. 2, pp. 270-273, April 1999

[7] F. Liefrink, G. de Jong, P. Teunissen, J.W. Heimeriks, A. Royset, A.A. Dyrseth, H. Schulze, R. Behr, J. Kohlmann, E. Vollmer, and J. Niemeyer, "Design of a bipolar Josephson array voltage standard for AC synthesis", Proc. BEMC1999, Brighton, UK, 59 (1999)

[8] The pulse-driven array is further investigated in the European JAWS project (contract no. G6RD-CT-2001-00599), which is coordinated by NMi-VSL. See www.jaws-project.nl for further information.

[9] O.A. Chevtchenko, H.E. van den Brom, E. Houtzager, G. de Jong, P. Teunissen and F. Liefrink, "Towards a Josephson arbitrary waveform synthesizer", to appear in IEE (2002)

[10] See, for example, "Delta-sigma data converters – theory, design and simulation", edited by S.R. Norsworthy, R. Schreier, and G.C. Temes (IEEE press, New York, 1996)

Polymer optical fibre network for feeding wireless LAN antenna stations

Ton Koonen (1) , Anthony Ng'oma (2) , Henrie van den Boom (3) , Idelfonso Tafur Monroy (4) ,
Peter Smulders (5) , Giok-Djan Khoe (6)
COBRA Institute, Eindhoven University of Technology
Den Dolech 2, NL 5612 AZ Eindhoven, The Netherlands (1) E-mail a.m.j.koonen@tue.nl ,
(2) E-mail a.ngoma@tue.nl , (3) E-mail h.p.a.v.d.boom@tue.nl , (4) E-mail i.tafur@tue.nl ,
(5) E-mail p.f.m.smulders@tue.nl , (6) E-mail g.d.khoe@tue.nl

Abstract

A novel method is presented to transport microwave signals over graded-index polymer optical fibre (GIPOF) networks feeding radio access points in high-capacity wireless LANs. It relies on optical frequency multiplying, by sweeping a laser wavelength over a number of free spectral ranges of a simple periodic optical filter at the access points. It enables a cost-effective system implementation, and easy upgrading by offering data signal transparency. Microwave frequencies at several tens of GHz carrying multi-point digital data signal constellation formats such as QPSK and QAM are achievable in GIPOF networks with a reach of several hunderds of metres.

Introduction

Wireless LANs are being installed at increasing pace in office and residential environments. Current products operate in the ISM 2.4 GHz band, offering data rates up to 11Mbit/s per microwave carrier. HiperLAN/2 systems exploit the 5.2 GHz band, transporting up to 54 Mbit/s per carrier, and future high-capacity wireless LANs may use microwave frequencies above 10 GHz to convey more than 100 Mbit/s per carrier. Along with this trend towards higher carrier frequencies and higher bitrates, the microwave radio cells are becoming smaller. This necessitates more antenna stations, and a more extensive in-house wiring to feed these stations with higher data rates. Next to that, it becomes attractive to consolidate the signal processing needed for mobility functions (such as macro-diversity and soft handover) at a central headend station. Thus the antenna stations can be relatively simple, and therefore more reliable and

(potentially) cheaper. To reap these benefits, however, the microwave signals should be carried transparently from the headend station to the antenna stations and vice versa. This will also ease future system upgrades. Optical fibre is well suited for transporting the microwaves, due to its very high bandwidth and low losses. By means of heterodyning optical carriers, transparent transport of the data signals via single-mode fibre has been demonstrated [1]. However, single-mode fibre is relatively costly to install in in-house environments. Perfluorinated graded-index polymeric optical fibre (GIPOF) is coming up as a promising medium which is easy to install due to its large core diameter and its flexibility, and is making fast progress towards lower losses (currently about 10 dB/km at 1300 nm) and higher bandwidths (currently around 1 GHz·km) [2], enabling short to medium-haul high bitrate data links [3]. However, heterodyning techniques are not feasible due to the multimode light guiding nature of the GIPOF.

This paper reports on a novel technique termed optical frequency multiplying, which allows carrying data signals on multi-GHz microwave carriers which stretch beyond the bandwidth of in-house GIPOF links (with lengths up to 500 meters, implying bandwidths up to 2 GHz).

Transporting microwave signals across a GIPOF link

The proposed system is based on a tree-and-branch polymer optical fibre network, with a wavelength-tunable laser diode at the headend site, and an optical filter with multiple equally-spaced passbands at the sites of the receivers, as shown in Fig. 1.
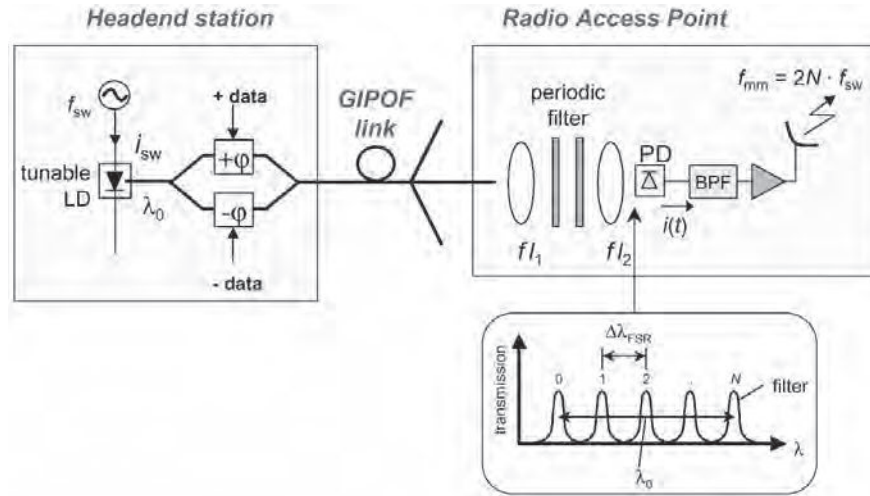
Fig. 1 Carrying microwave signals through a Polymer Optical Fibre network

In the Headend station, the wavelength of the tunable laser diode is swept with a sweep frequency f_{sw}, while keeping its light output power nearly constant. Subsequently, the data signal is impressed on this wavelength-swept optical carrier by means of a low-chirp external intensity modulator (such as a differentially-driven Mach-Zehnder modulator).

After traveling through the point-to-multipoint GIPOF network, the signal arrives at a Radio Access Point. It passes through the periodic optical bandpass filter, and then impinges on a high-frequency photodiode. When the wavelength-sweep of the signal is adjusted to encompass an integer multiple N of the Free Spectral Range (FSR) of the optical bandpass filter, each sweep of the signal generates $2N$ intensity fluctuations at the photodiode, and thus a microwave signal with a frequency f_{mm} which equals $2N$ times the sweep frequency f_{sw}. This periodic optical filtering process, however, does not affect the data intensity modulation (as long as the data rate is lower than the sweep frequency f_{sw}).

Thus a transparent transport of the data signal is accomplished. An electrical bandpass filter after the photodiode suppresses the unwanted harmonics of the microwave signal, and reduces the noise. Subsequently, the signal is fed to the antenna, and the microwave signal carrying the data is radiated to the end user terminals.

The signal data rate and laser sweep frequency are limited by the modal dispersion in the GIPOF link. For link lengths up to 500 meters, sweep frequencies up to 2 GHz should be feasible. It should be noted that the microwave frequency generated is not limited by these two factors, as the optical multiplication factor is only determined by the ratio between the sweep range of the optical frequency and the FSR of the periodic optical filter.

The periodic optical bandpass filter can be advantageously implemented by means of a Fabry-Perot (FP) filter, which can be inserted between the GIPOF and the photodiode using a lens system for collimating the optical beam and imaging the large fibre core on the small light-sensitive area of the photodiode. Such an FP filter consists of simply two parallel optical reflective plates with a small spacing, and can be realised at low cost in a compact size.

To get a nice periodic microwave frequency signal, it is preferable to sweep the laser wavelength as a triangular function of time, as illustrated in Fig. 2. The resulting periodic microwave signal waveform $i(t)$ at the output of the photodiode in the Radio Access Point will then have the same shape as the FP transmission curve. It can be expanded in a Fourier series, of which the n-th harmonic (with frequency $n \cdot 2N \cdot f_{sw}$) has a relative amplitude $2 \cdot R^n (1 - R)/(1 + R)$, according to

$$i(t) = \frac{i_0}{1 + F \cdot \sin^2(2\pi N f_{sw} t)} =$$

$$i_0 \cdot \frac{1-R}{1+R} \left\{ 1 + 2 \sum_{n=1}^{\infty} R^n \cos(4\pi n N f_{sw} t) \right\}$$

The powers of these harmonics thus clearly depend on the reflectivity R of the plates of the FP, as shown in Fig. 3. The fundamental first harmonic
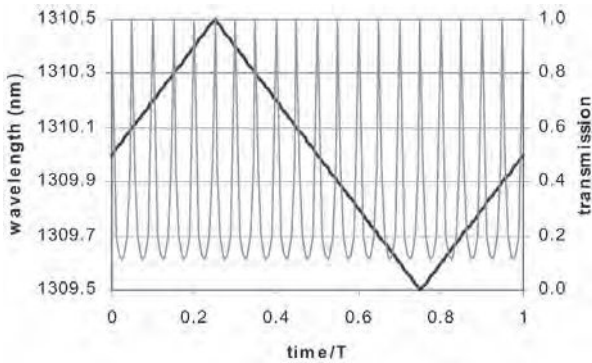
Fig. 2 Generated microwave signal using a triangular wavelength sweep at the laser transmitter and a Fabry Perot periodic optical filter at the receiver

$2N \cdot f_{sw}$ reaches its maximum for $R = 0.41$, but this optimum is not very sharp, so that the value of R is not very critical.

When sweeping the laser wavelength as a sinusoidal function of time, also a periodic microwave signal will be generated, but next to the desired harmonics $n \cdot 2N \cdot f_{sw}$ a lot of spectral lines spaced at twice the sweep frequency $2 \cdot f_{sw}$ will be present.

System performance simulations

The performance of the proposed system has been simulated using the Virtual Photonics Inc. software package. Assumed is a triangular wavelength sweep at frequency $f_{sw} = 900$ MHz over an optical frequency range of 28.8 GHz (amounting to a wavelength range of 0.16 nm), and a Fabry-Perot filter with Free Spectral Range $FSR = 9.6$ GHz (corresponding to a 15.6 mm plate spacing) and plate reflectivity $R = 20\%$ (which is lower than optimum, but provides a good compromise between strength of the fundamental frequency and suppression of the higher harmonics). The optical frequency multiplication factor obtained is $2N = 6$, thus yielding a 6 x 900 MHz = 5.4 GHz carrier frequency.

Fig. 3 Strength of the various harmonic components in the generated microwave signal

Fig. 4 shows the spectrum of the generated unmodulated microwave carrier.

Adjusting the central frequency of the electrical bandpass filter allows also operating at a higher harmonic frequency, e.g. 10.8 GHz, while maintaining data signal transparency. Assuming an 225 Mbit/s on/off keyed data signal and a third-order Bessel electrical bandpass filter with a FWHM bandwidth of 315 MHz (140% of the data rate; it may go up to $4 \cdot f_{sw}$) centered at 5.4 GHz, a nice signal waveform at the filter output is obtained, illustrating the transparency for the data signal; see Fig. 5. Also, by adjusting the electrical filter's central frequency, at the second harmonic at 10.8 GHz a nice signal waveform is obtained. The shape of the data signal remains clearly unaltered, which underlines the potential of the system for upgrading to even higher microwave frequencies while maintaining data signal transparency.

Fig. 4 Spectrum of unmodulated microwave signal at the output of the photodiode, before the bandpass filter

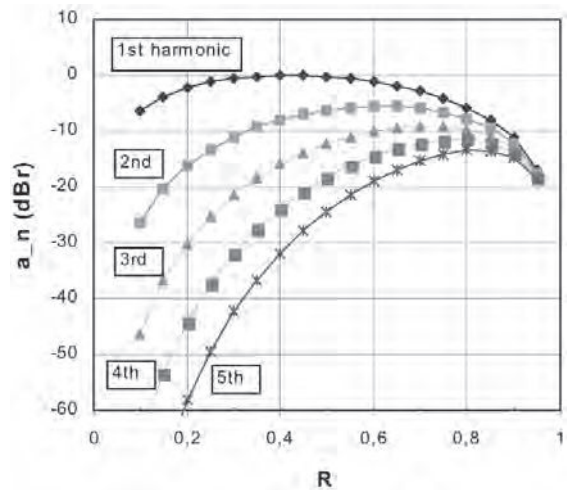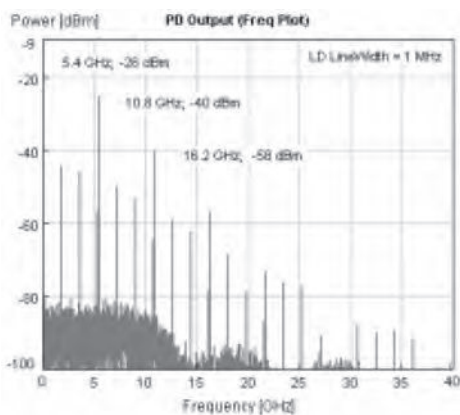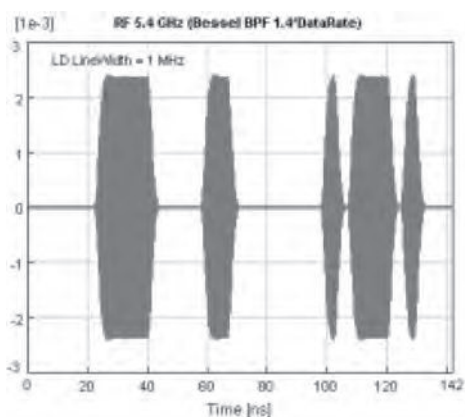Fig. 5 Microwave signal on-off modulated with 225 Mbit/s data, at output of the bandpass filter centered at 5.4 GHz

As shown by simulations, also other data signal multi-point constellation formats, such as QPSK and x-level QAM, can be carried by putting these on a subcarrier wave which is subsequently fed to the Mach-Zehnder device modulating the optical-wavelength swept laser signal at the headend site. The subcarrier frequency should be below the optical sweep frequency, but higher than the data rate.

Extension to bidirectional operation

The system is extendable to a half-duplex bi-directional system, as shown in Fig. 6. In the silent downstream periods, the unmodulated microwave carrier signal obtained in the antenna base station can be used for downconverting to baseband the signal which is received at the microwave frequency at the antenna for upstream transmission. This baseband signal is subsequently modulated on a low-cost laser diode at the antenna site, and sent upstream along the GIPOF network. Preferably the upstream laser diode operates at a different wavelength than the downstream laser diode at the headend site, and simple wavelength multi/demultiplexers are used at both ends to improve the directivity and thus sufficiently reduce near-end crosstalk.

Conclusions

A novel method for application in wireless LANs has been presented to carry microwave signals over graded-index polymer optical fibre networks, surpassing their limited bandwidth. This optical frequency multiplying method relies on wavelength sweeping an optical source at the headend station across the intensity transfer function of a periodic optical filter at the antenna base stations. It combines the installation easiness of polymer fibre with the consolidation of mobility functions at the headend and simplification of the antenna stations.

Microwave carrier frequencies significantly beyond the bandwidth of the polymer optical fibre can be realised; frequencies above 60 GHz are realistically obtainable in a POF network with a reach of up to 500 m (having a bandwidth up to 2 GHz), by e.g. sweeping the laser wavelength at a rate of 1 GHz over a range of 1.2 nm (150 GHz) and using at the antenna site a periodic filter with FSR = 5 GHz followed by a 60 GHz photodiode. The system is capable of transporting various signal modulation formats, such as ASK, BPSK, QPSK and x-level QAM.

This approach may enable cost-effective installation of high-capacity wireless LANs, and easy upgrading by offering data signal transparency.

Acknowledgement

References

[1] R.P. Braun et al., "Optical feeding of base stations in millimeter-wave mobile communications", Proc. of ECOC'98, Madrid, Sep. 20-24, 1998, Vol. 1, pp. 665-666

[2] Chikafumi Tanaka, "Progress of perfluorinated GI-POF", Proc. of ECOC'01, Amsterdam, Sep. 30 – Oct. 4, 2001, Vol. 1, pp. 66-67

[3] Ton Koonen et al., "Broadband data communication techniques in POF-based networks", Proc. of ECOC'01, Amsterdam, Sep. 30 – Oct. 4, 2001, Vol. 1, pp. 14-15

Fig. 6 Extension to half-duplex bidirectional system
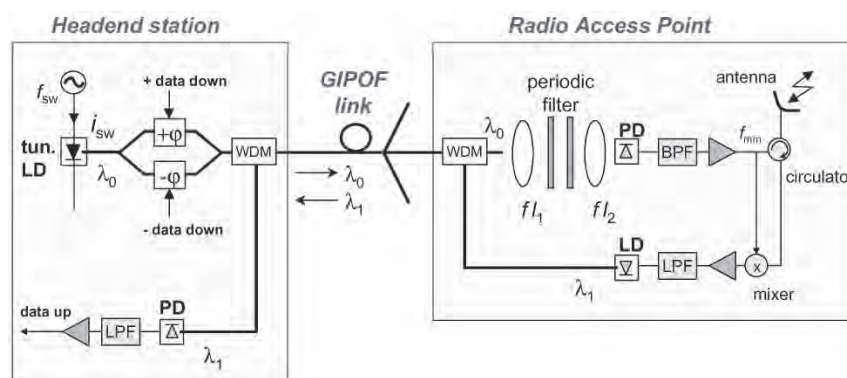
Solution and stability analysis of a new integral equation for the transient scattering by a flat, rectangular conducting plate

Jos G.A. van Riswick [1] and *Anton G. Tijhuis* [2]
[1] *Eindhoven University of Technology, Faculty of Electrical Engineering,*
P.O. Box 513, 5600 MB Eindhoven, the Netherlands,
e-mail: [2] *As* [1] *above, but e-mail: A.G.Tijhuis@tue.nl*

Abstract

In this contribution, we present a new Hallén-type formulation for scattering by a two-dimensional, perfectly conducting rectangular plate. We derive two coupled integral equations for the components of the induced surface current, which are solved by marching on in time. The numerical results may exhibit instabilities, but the solution can be stabilized in various ways. To arrive at a more detailed understanding of the stability problem, we reformulate the computation in a combination of a finite-difference time-domain computation and the solution of two scalar integral relations which no longer contain space and time differentiations. Both procedures are coupled via the boundary conditions at the edges of the plate. As a reference result, we consider the transient excitation of an infinite flat plate by a pulsed, vertical electric dipole, for which the unknown vector potential and the induced surface currents are available in closed form.

Introduction

The electric-field integral equation (EFIE) is a common tool for determining scattered or radiating fields emanating from a perfectly conducting, open surface. In this type of approach the induced surface current and/or charge density are solved from the integral equations, and, subsequently, the scattered electromagnetic field is determined at any given point by evaluating the integrals in a conventional integral representation. Advantages of this approach are that the radiation condition is accounted for inherently, and that only two-dimensional surface currents and/or charges need to be computed over the area of the scattering surface, instead of three-dimensional electromagnetic fields over a volume surrounding that surface.

When the EFIE is solved directly in the time domain, instabilities are often observed in the computed results. Numerical experiments for a number of two-dimensional transient-scattering problems [1] as well as for perfectly conducting surfaces indicate that the occurrence of such unstable solutions is enhanced by the presence of space derivatives in these equations. In particular, the manner in which these derivatives are approximated in the space discretization has a considerable influence on the stability of the computational solutions. To investigate this observation in more detail, we consider the "canonical" problem of a rectangular, flat plate excited by a pulsed incident field. The role of the space derivatives is isolated from the complete computation by reformulating the procedure in three steps. First, we reduce the original EFIE to a Hallén-type integral equation, which consists of two coupled, scalar integral equations for the transverse currents $J_x(x, y, t)$ and $J_y(x, y, t)$. This step was inspired by the success of using Hallén's integral equation for the total current $I(z, t)$ along a straight conducting thin wire in time-domain computations [2]. Marching-on-in-time schemes based on our new integral equation are still unstable, but can be stabilized with the aid of time averaging.

Therefore, the second modification in our approach is to reformulate the integral equations in terms of two coupled differential equations that can be solved by a finite-difference time-domain scheme, and two uncoupled scalar integral equations, where the current densities $J_x(x, y, t)$ and

$J_y(x, y, t)$ are resolved from the corresponding components of a vector potential $A(x, y, t)$. Here, we found our inspiration in a similar treatment of the EFIE in [3]. A straightforward discretization of the differential equations results in a scheme that satisfies the well-known Courant stability criterion for two-dimensional wave propagation. The scalar integral equation is then solved by marching on in time, as described in [3].

For the case where the flat plate is infinite, both parts of the computation can be validated independently, by comparing numerical results with closed-form expressions for the field excited by a horizontally or vertically polarized, pulsed electric point dipole located above the plate. When the plate has finite dimensions, coupling occurs via the boundary conditions at its edges. This means that the two parts of the computation must be combined, and that the stability of the entire scheme depends on the implementation of these boundary conditions.

Formulation of the problem

A pulsed plane wave is incident on a two-dimensional, perfectly conducting rectangular plate as shown in Fig. 1. The Cartesian coordinate system is chosen such that the plate is located at $0 < x < a$, $0 < y < b$, and $z = 0$. The surrounding homogeneous, linearly and instantaneously reacting, isotropic medium has permittivity ε and permeability μ. We start from the standard form of the electric-field integral equation

$$\left(\nabla_T \nabla_T \cdot -\frac{1}{c^2}\partial_t^2\right)A(\mathbf{r}_T, t) = -\varepsilon\partial_t E_T^i(\mathbf{r}_T, t), \quad (1)$$

which holds for $\mathbf{r}_T$ on the plate. In (1), the subscript $_T$ stands for transverse, and the vector potential $A(\mathbf{r}_T, t)$ is related to the unknown surface current density $J_S(\mathbf{r}_T, t)$ in the plane $z = 0$ according to

$$A(\mathbf{r}_T, t) = \int_0^a dx' \int_0^b dy' \frac{J_S(\mathbf{r}'_T, t - R/c)}{4\pi R}, \quad (2)$$

Fig. 1. Pulsed plane wave incident on a flat rectangular plate.
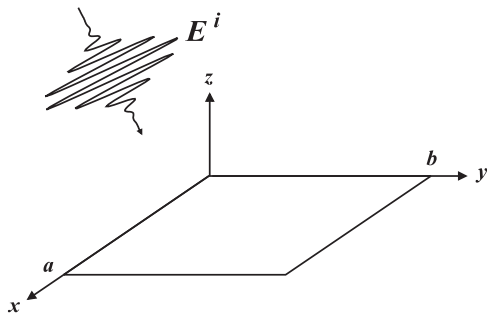
with $R = |\mathbf{r}_T - \mathbf{r}'_T|$ and $c = 1/\sqrt{\varepsilon\mu}$. The aim of the computation is to determine $J(\mathbf{r}_T, t)$ for $0 < x < a$ and $0 < y < b$ for a given behavior of the transverse incident field $E_T^i(\mathbf{r}_T, t)$. Once this surface current is known, it can be treated as a "secondary" source that generates the electromagnetic field scattered by the plate.

Hallén-type integral equation

As mentioned in the introduction, numerical differentations with respect to space and time are often the source of instabilities in time-domain computations. Therefore, they should be avoided as much as possible. To this end, we break up (1) into its x- and y-components. Since we restrict ourselves to the plane $z = 0$, we may replace $\mathbf{r}_T$ by the corresponding transverse coordinates x and y. This reduces (1) to a pair of coupled scalar electric-field integral equations:

$$\left(\partial_x^2 - \frac{1}{c^2}\partial_t^2\right)A_x(x, y, t) + \partial_x\partial_y A_y(x, y, t)$$
$$= -\varepsilon\partial_t E_x^{inc}(x, y, t), \quad (3)$$

$$\left(\partial_y^2 - \frac{1}{c^2}\partial_t^2\right)A_y(x, y, t) + \partial_y\partial_x A_x(x, y, t)$$
$$= -\varepsilon\partial_t E_y^{inc}(x, y, t), \quad (4)$$

In analogy with the case of a straight thin-wire segment, we identify the differential operators in the first terms on the lefthand sides as one-dimensional wave operators, that can be evaluated with the aid of a one-dimensional Green's function technique. This results in

$$A_x(x, y, t) = -\frac{1}{2}\int_0^a dx' \text{sgn}(x - x')\,\partial_y A_y(x', y, t - |x - x'|/c)$$
$$+ \frac{Y}{2}\int_0^a dx' E_x^{inc}(x', y, t - |x - x'|/c) + F_0(t - x/c, y) + F_a(t - (a - x)/c, y),$$
$$\quad (5)$$
$$A_y(x, y, t) = -\frac{1}{2}\int_0^b dy' \text{sgn}(y - y')\,\partial_x A_x(x, y', t - |y - y'|/c)$$
$$+ \frac{Y}{2}\int_0^b dy' E_y^{inc}(x, y', t - |y - y'|/c) + G_0(t - y/c, x) + G_b(t - (b - y)/c, x).$$

In (5), the time signals $F_0(t, y)$, $F_a(t, y)$, $G_0(t, x)$ and $G_b(t, x)$ correspond to homogeneous solutions of the relevant one-dimensional wave equations. To fix these signals, we need to augment the pair of integral equations in (5) with the boundary conditions

$$J_x(0, y, t) = 0; J_x(a, y, t) = 0; J_y(x, 0, t) = 0; J_y(x, b, t) = 0,$$
$$(6)$$

which follow from the observation that $J_S(x, y, t)$ is tangential at the edges of the plate.

Our first approach was to solve the system of equations formed by (5) and (6) by *marching on in time*.

In the space discretization, the plate is subdivided into $L \times M$ cells with dimensions $\Delta x = a/L$ and $\Delta y = b/L$. The unknown currents are approximated by rooftop functions, and the integral equation is collocated on a staggered grid, at $x = \ell\Delta x$ and $y = (m + \frac{1}{2})\Delta y$, and $x = (\ell +\frac{1}{2})\Delta x$ and $y = m\Delta y$, respectively. This involves approximations of the form

$$J_x(x,y,t) = \sum_{\ell=1}^{L-1} \sum_{m=0}^{M-1} J_x[\ell,m;t]\, \Lambda(x - \ell\Delta x; \Delta x)\, \Pi(y - [m + \tfrac{1}{2}]\Delta y; \Delta y), \quad (7)$$

where $\Delta x = a/L$, $\Delta y = b/M$, $\Lambda(\xi; h)$ is a triangle function of width $2h$ and $\Pi(\xi; h)$ is a rectangle function of width h. In (7), the first two boundary conditions of (6) are accounted for by leaving out the terms with $\ell = 0$ and $\ell = L$. Similarly, its counterpart for $J_y(x, y, t)$ satisfies the last two conditions of (6). In both cases, the relevant integral equation from (5) is collocated as well at these points to allow the determination of the unknown time signals. Finally, the time coordinate is discretized with time step Δt. The time retardation in the the delayed current $J_x(x, y, t - R/c)$ is handled by linear interpolation in time, and the differentiations with respect to y and x in (5) are evaluated via integration by parts. The resulting integrals over x' and y' in each cell can now be evaluated in closed form. The first integrals over x' and y' in the right-hand sides of (5) are approximated by a repeated midpoint rule, while the second ones are evaluated in closed form. Depending on the choice of the time step, the space-time discretization described above results in an explicit or an implicit scheme. In the latter case, a sparse matrix equation must be solved at each discrete time step.

As in the case of the original time-domain equation (1), the solution may exhibit instabilities. In our opinion, these instabilities can be explained from the fact that, by choosing a fixed space discretization, one inherently introduces an increasing error for increasing frequencies. Especially near the Nyquist frequency, this may lead to the introduction of spurious poles outside the unit circle in the discretized-frequency plane. The corresponding residual contributions are alternating, exponentially increasing time sequences. Based on this interpretation, several procedures seem available for stabilizing the solution. Until now, we have had partial success with smoothing the result after each time step, and with choosing a larger time step and using an implicit scheme. Smoothing does have a stabilizing effect, but generally affects the accuracy of the solution. Moreover, refining the discretiza-

tion may bring back the instabilities. Using an implicit scheme is not as effective as we expected. The occurrence of instabilities depends critically on the condition of the system matrix of the linear system of equations that must be solved for each time step to obtain the field at that instant. This system matrix, in turn, depends directly on the manner in which the space-time integral equation is discretized.

Finite-difference formulation

A closed-form stability analysis of the procedure given in the previous chapter is, to our knowledge, not available. Even for the case of an infinite plate, generalizing the Von Neumann procedure that is customary for finite-difference calculations is too complicated. Therefore, we reformulate the integral equations in (5) in such a way that the vector potential can be solved from a system of differential equations with the aid of finite differences. This part of the time-marching scheme can then be subjected to a Von Neumann stability analysis. This leaves the calculation of the the induced surface currents from the calculated potential. However, at least the consequences of the numerical differentiations in the scheme can be understood in this manner. For the infinite-plate problem, the analysis provides exact answers since we do not have to deal with boundary conditions. For a finite plate, the results are identical to those for the infinite plate until the induced currents reach the edge of the spatial grid. From that instant on, boundary conditions must be imposed and the two parts of the computation can no longer be carried out independently.

To arrive at the desired scheme, we introduce the auxiliary quantities

$$R_x(x,y,t) = \tfrac{1}{2}\int_0^b dy'\, \mathrm{sgn}(y - y')A_z(x,y',t - |y - y'|/c),$$

$$R_y(x,y,t) = \tfrac{1}{2}\int_0^a dx'\, \mathrm{sgn}(x - x')A_y(x',y,t - |x - x'|/c),$$

$$Q_x(x,y,t) = \tfrac{1}{2}\int_0^b dy'\, A_x(x,y',t - |y - y'|/c),$$

$$Q_y(x,y,t) = \tfrac{1}{2}\int_0^a dx'\, A_y(x',y,t - |x - x'|/c) \quad (8)$$

Partial differentiation of the first and third lines of (8) with respect to y, and of the second and fourth lines of (8) with respect to x directly results in the first-order partial differential equations

$$\partial_y R_x(x,y,t) + \tfrac{1}{c}\partial_t Q_x(x,y,t) = A_x(x,y,t),$$
$$\partial_x R_y(x,y,t) + \tfrac{1}{c}\partial_t Q_y(x,y,t) = A_y(x,y,t), \quad (9)$$

$$\partial_y Q_x(x,y,t) + \tfrac{1}{c}\partial_t R_x(x,y,t) = 0,$$

$$\partial_x Q_y(x,y,t) + \tfrac{1}{c}\partial_t R_y(x,y,t) = 0.$$

The two coupled Hallén-type integral equations given in (5) now reduce to

$$A_x(x,y,t) = -\partial_y R_y(x,y,t) + P_x(x,y,t)$$
$$\qquad + F_0(t - x/c, y) + F_a(t-(a-x)/c, y),$$

$$A_y(x,y,t) = -\partial_x R_x(x,y,t) + P_y(x,y,t) \qquad (10)$$
$$\qquad + G_0(t - y/c, x) + G_b(t-(b-y)/c, x).$$

where $P_x(x, y, t)$ and $P_y(x, y, t)$ are known functions that depend on the incident field:

$$P_x(x,y,t) = \tfrac{\gamma}{2}\int_0^a dx'\, E_x^{inc}(x',y,t-|x-x'|/c),$$
$$P_y(x,y,t) = \tfrac{\gamma}{2}\int_0^b dy'\, E_y^{inc}(x,y',t-|y-y'|/c). \qquad (11)$$

The system of partial differential equations can be consistently translated into a finite difference scheme by approximating the derivatives using the central difference rule, and using a grid staggered in space and time.

In formulating the difference equations, we use a short-hand notation to indicate the approximated version of the unknown quantities, e.g.,

$$A_x[\ell, m, n] = A_x(\ell\,\Delta x, m\,\Delta y, n\,\Delta t); \qquad (12)$$

where ℓ, m and n denote integer numbers, and where Δx, Δy and Δt are the spatial cell sizes in the x- and y-directions, and the time step. To arrive at a consistent scheme, we evaluate the approximated quantities $A_x[\ell, m+\tfrac{1}{2}, n]$, $A_y[\ell+\tfrac{1}{2}, m, n]$, $R_x[\ell, m, n]$, $R_y[\ell, m, n]$, $Q_x[\ell, m+\tfrac{1}{2}, n+\tfrac{1}{2}]$, $Q_y[\ell+\tfrac{1}{2}, m, n+\tfrac{1}{2}]$. By sampling in this manner, we arrive at an FDTD scheme on a Yee-type grid. The spatial part of the sampling is illustrated in Figure 2.

The resulting finite difference scheme can be subjected to a Von Neumann stability analysis to derive a stability condition for the scheme. We arrive at the usual Courant condition for two-dimensional propagation:

$$c\Delta t \leq 1/\sqrt{1/\Delta x^2 + 1/\Delta y^2} \qquad (13)$$

As can be observed from Figure 2, the sampling of A_x and A_y is consistent with the space discretization for the original Hallén-type equations (5). This means that we can use the same procedure to discretize the equations for obtaining J_x and J_y from the x- and y-components of (2). In the space discretiza-
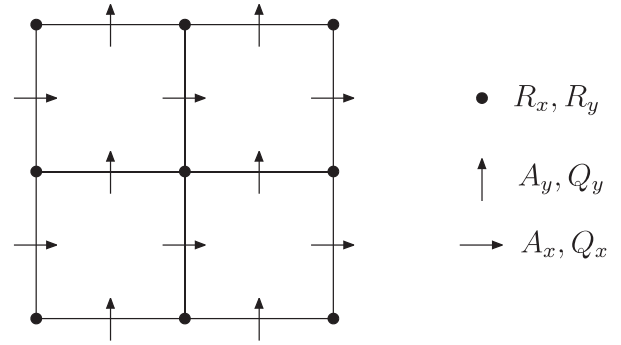
Fig.2. Four cells of the finite difference grid.

$\bullet\quad R_x, R_y$

$\uparrow\quad A_y, Q_y$

$\rightarrow\quad A_x, Q_x$

tion, we have introduced one refinement. To ensure that the retarded time $t' = t - R/c$ is as much as possible in the correct "time zone" $(n - k - 1)\Delta t < t' < (n - k)\Delta t$, we carry out the time interpolation and the integration over x' and y' in (2) over a sub-grid in each cell prior to the marchingon-in-time computation. In this manner, we allow each spatial cell to cover more than one "time zone", which has been demonstrated in the acoustic case to contribute to the stability of the solution [4].

Finally, it should be mentioned that each step of the procedure described above can be verified independently for the special case of excitation by a vertical electric dipole located above the center of the plate. Until the currents reach the end of the plate, the solution is identical to that for an infinite plate, for which $A_{x,y}$ and $J_{x,y}$ are available in closed form. This means that each step of the procedure can be validated independently. Results cannot be included here because of space limitations, but will be presented and discussed at the conference.

References

[1] A.G. Tijhuis, *Electromagnetic Inverse Profiling; Theory and Numerical Implementatio*n, VNU Science Press, Utrecht, the Netherlands, 1987, Sections 3.2 and 3.5.

[2] A.G. Tijhuis, Z.Q. Peng and A. Rubio Bretones, "Transient excitation of a straight thin-wire segment: a new look at an old problem", *IEEE Trans. Antennas Propagat.*, vol. 40, 1132-1146, 1992.

[3] B.P. Rynne and P.D. Smith, "Stability of time marching algorithms for the electric field integral equation", *J. of Electromagnetic Waves and Application*s, vol. 4, 1181-1205, 1990.

[4] G.C. Herman, "Scattering of transient acoustic waves by an inhomogeneous obstacle", *J. Acoust. Soc. Am.*, vol. 69, 909–915, 1981.

Performance evaluation of an OOK coherence multiplex receiver based on 4 × 4 phase diversity detection

Arjan Meijerink [(1)], *Geert Heideman* [(2)], *Wim van Etten* [(3)]

[(1)] *Telecommunication Engineering Group, Faculty of Electrical Engineering,*

University of Twente, P.O. Box 217, 7500 AE, Enschede, The Netherlands, a.meijerink@ieee.org

[(2)] *As (1) above, but E-mail: g.h.l.m.heideman@el.utwente.nl*

[(3)] *As (1) above, but E-mail: etten@ieee.org*

Abstract

Coherence multiplexing (CM) is a relatively cheap method for multiplexing multiple channels onto a fiber-optic link. Most previously published CM systems use either single-ended or balanced detection, which requires phase-locking for a stable output signal. Recently, we proposed a scheme in which the receiver output signal is stabilized by a phase diversity network. In this paper, the interferometric noise-limited performance of a CM receiver based on 4 × 4 phase diversity detection is analyzed and compared to a receiver based on balanced detection. The results will show that phase diversity introduces only a slight degradation of the transmission capacity of the system.

Coherence multiplexing (CM)

Coherence multiplexing (CM) is a form of CDMA which is especially suited for optical transmission [1]. Although CM cannot compete with WDM as far as transmission rates are concerned, it might be favourable from a cost point of view, as broadband light sources (for instance LEDs) and only simple components are required for crosstalk-free transmission. Therefore, CM is particularly suitable for small-scale networks like LANs and access networks. CM is based on the principle of distinguishing between coherent and incoherent mixing of lightwaves, as illustrated in Fig. 1.

The idea is that each transmitter launches both a BPSK modulated version and an unmodulated version of the broadband carrier into the common fiber. These two carriers are made mutually incoherent (uncorrelated) by delaying them with respect to each other by a timeshift T_{tr} which is much larger than the coherence time of the source τ_c. In the receiver, the correct channel can be selected by mixing the received signal with the same signal being delayed by a timeshift T_{re}. Mixing is performed by a balanced detector, which consists of a 2 × 2 coupler and two photodiodes. If $T_{re} = T_{tr}$ then the lightwave taking the upper path in the transmitter and the lower path in the receiver mixes coherently with the lightwave taking the lower path in the transmitter and the upper path in the receiver, as their mutual time delay is zero. Since one of these lightwaves is modulated, the mixing product is an antipodal baseband signal proportional to the modulating signal $m(t)$. If the delays of all the transmitters are spaced apart much more than the coherence time of the sources, then it can be simply verified that all the lightwaves from interfering transmitters mix incoherently, resulting

Figure 1: A coherence multiplex system with one transmitter and one receiver
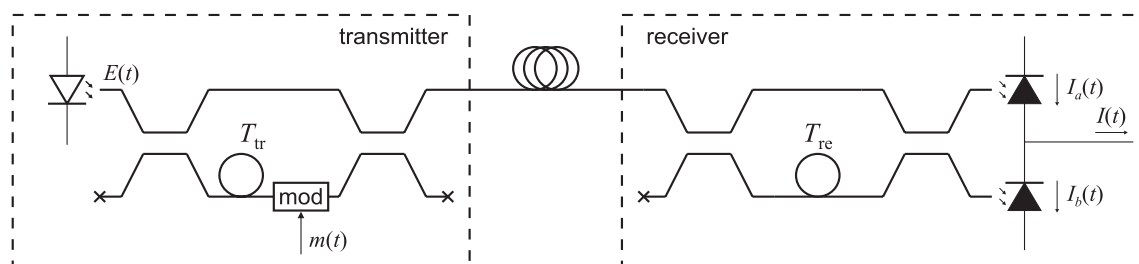
in broadband interferometric noise. Moreover, the coherent mixing term suffers from source intensity noise. Both noise currents have a very broad power spectral density function which is proportional to the square of the received power. The power spectral densities of shot noise and thermal receiver noise are proportional to and independent of the received power, respectively. Hence, for large received powers, they can be neglected. Assuming that the complex envelope of the field emitted by the broadband source can be modelled as a circular complex Gaussian process with a Gaussian spectral profile, and that all the fields in the receiver have matched polarization states, the signal-to-noise ratio after matched filtering can be shown to be [1]

$$SNR = \frac{2}{4M^2+2M+1} \frac{T_b}{\tau_c} = \frac{\sqrt{\frac{2\pi}{\ln 2}}}{4M^2+2M+1} \frac{\Delta f}{R_b} \quad (1)$$

where M is the number of active users, T_b is the bit-time of the modulating signal $m(t)$, Δf is the 3 dB linewidth of the source and R_b is the bitrate. As the matched filter bandwidth will generally be much smaller than the bandwidth of the noise, the decision samples can be assumed to be Gaussian distributed, so the bit error rate is given by

$$P_e \approx \frac{1}{\sqrt{2\pi}} \int_{\sqrt{SNR}}^{\infty} \exp\left(-\frac{x^2}{2}\right) dx \equiv Q\left(\sqrt{SNR}\right) \quad (2)$$

Stability issue

The problem with this balanced receiver is that the coherent lightwaves have to be mixed exactly in phase in order to achieve constructive interference. Therefore, even a small drift in the delay in either the transmitter or receiver will introduce a drop in the amplitude of the output signal, by a factor $\cos\left(2\pi f_c (T_{tr} - T_{tr})\right)$, where f_c is the carrier frequency of the light [2]. In most publications on CM, this practical problem is solved by phase-locking the coherent lightwaves. This can be done by applying a feedback loop from the detected signal to the delay T_{re}, which adapts the refractive index, for example by means of the thermo-optic or electro-optic effect [3]. Recently, we proposed how stabilized detection without phase-locking can be

performed using a 3 × 3 phase diversity scheme [2]. Phase diversity is a detection method which has been successfully applied in numerous types of coherent optical systems [4]. In this paper, a coherence multiplex receiver based on a 4 × 4 phase diversity network is introduced. Capacity bounds of the resulting system will be given, and compared to the case in which balanced detection was used.

Performance of an ook 4 × 4 phase diversity receiver

Consider the coherence multiplex receiver based on a 4 × 4 phase diversity network, as given in Fig. 2. In this receiver, the balanced mixer is replaced by a 4 × 4 optical hybrid (for instance a multimode interference coupler) and two differential pairs of photodiodes. The geometry of the hybrid is assumed to be such that the power of the input signals is equally divided over the output ports, and moreover, that the mixing phases are given by ϕ, $\phi + \frac{\pi}{2}$, and $\phi + \pi$, where ϕ is an arbitrary phase that depends both on the phase difference between the input signals (which changes with $|T_{tr} - T_{re}|$ and on the absolute phase transfer of the hybrid.

As a result, the output currents of the differential photodiode pairs $I_I(t)$ and $I_Q(t)$ both consist of desired signals $I_{I,s}(t)$ and $I_{Q,s}(t)$, respectively, and broadband noise $I_{I,n}(t)$ and $I_{Q,n}(t)$, respectively. It can be shown that the desired signals are given by $m(t) A \cos \phi$ and $m(t) A \sin \phi$, respectively, where the amplitude A incorporates transmitted power, splitting and coupling losses, and the responsivity of the photodiodes. To minimize the degradation due to the noise, both signals are first matched filtered by the low-pass filters, before they are squared and added, which results in an output signal that does not depend on ϕ, as the difference in mixing phase is $\frac{\pi}{2}$ radians. Therefore, it is not possible to detect BPSK modulated signals using this phase diversity receiver. This can be solved by replacing the BPSK modulation in Fig. 1 by on-off keying (OOK), which can be performed by directly

Figure 2: A coherence multiplex received based on a 4x4 phase diversity network
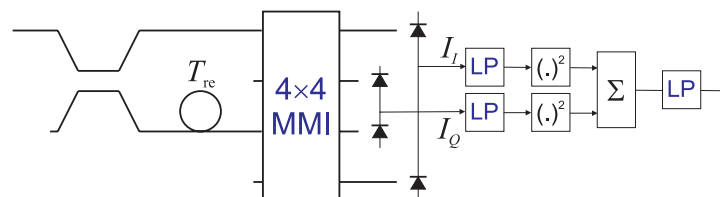
modulating the source. Since transmitting a '0'-bit incorporates switching off the source, the variance of the interferometric noise depends on the number of users that are simultaneously transmitting a '1'-bit; therefore the signal-to-noise ratio can be considered as a random process $\gamma(t)$ which is varying with time. The distribution of $\gamma(t)$ can be determined by assuming that the received signals from both the matched transmitter and the interfering transmitters are bit-synchronized, such that for a particular bit k, the signal-to-noise ratio is a discrete random variable γ_k that can take one out of M possible values. All transmitters are assumed to transmit '0' and '1' bits with an equal probability of ½, so the number of interfering transmitters N_k that is transmitting a '1'-bit, is binomially distributed. As a result, the average bit error probability can be calculated as follows:

$$P_e \approx \sum_{n=0}^{M-1} P_{e|N_{k=n}} P[N_k=n] = \left(\frac{1}{2}\right)^{M-1} \cdot \sum_{n=0}^{M-1} P_{e|N_{k=n}} \binom{M-1}{n} \quad (3)$$

Now consider the two mixing currents $I_I(t)$ and $I_Q(t)$. Both currents consist of a desired part $I_{I,s}(t)$ and $I_{Q,s}(t)$, respectively, interferometric noise $I_{I,in}(t)$ and $I_{Q,in}(t)$, respectively, and source intensity noise, $I_{I,sin}(t)$ and $I_{Q,sin}(t)$, respectively. As the complex envelopes of the electrical fields corresponding to the source lightwaves are considered as circular complex Gaussian processes with a spectral profile that is symmetric around the carrier frequency, the quadrature components of the electrical field are independent. Therefore, the interferometric noise components $I_{I,in}(t)$ and $I_{Q,in}(t)$ can be assumed to be uncorrelated. Now let I_k and Q_k denote the output samples of the matched filters for a particular bit k. Then it can be shown that I_k and Q_k contain information terms $I_{s,k} \equiv E[I_k] = m_k A \cdot T_b \cos\phi$ and $Q_{s,k} \equiv E[Q_k] = m_k A \cdot T_b \sin\phi$ respectively, and source intensity noise terms $I_{sin,k} = A_{sin,k} \cos\phi$ and $Q_{sin,k} = A_{sin,k} \sin\phi$, respectively, where $A_{sin,k}$ is zero-mean Gaussian with variance $\sigma^2_{sin,k} = m_k A^2 T_b \tau_c$. Finally, the interferometric noise terms $I_{in,k}$ and $Q_{in,k}$ are mutually uncorrelated zero-mean Gaussian distributed with equal variance $\sigma^2_{in,k} = \frac{1}{2}(4N_k^2 + (8m_k+2)N_k + 5m_k)A^2 T_b \tau_c$, where m_k is the corresponding information bit (which is either 0 or 1). As $A_{sin,k}$, $I_{in,k}$ and $Q_{in,k}$ are jointly Gaussian and mutually uncorrelated, they are independent. Now let S_k denote the output signal of the phase diversity receiver at the optimum sampling instant, so S_k is given by

$$S_k = I_k^2 + Q_k^2 = \left((m_k A \cdot T_b + A_{sin,k})\cos\phi + I_{in,k}\right)^2 + \left((m_k A \cdot T_b + A_{sin,k})\sin\phi + Q_{in,k}\right)^2 \quad (4)$$

When a binary '0' is transmitted, S_k can be proven to have a probability density function f_{S_k} which is central chi-squared with two degrees of freedom. If the detection threshold is denoted by s_{th}, then the probability of error for a binary '0' can be proven to be

$$P_{e|m_k=0, N_k=n} = \int_{s_{th}}^{\infty} f_{S_k|m_k=0, N_k=n}(s)ds$$
$$= \exp\left(-\frac{S_{th}}{(4n^2 + 2n)A^2 T_b \tau_c}\right) \quad (5)$$

For large signal-to-noise ratios, the output signal S_k in case of a binary '1' can be proven to be approximately non-central chi-square distributed with one degree of freedom, and the probability of a bit error in that case is

$$P_{e|m_k=0, N_k=n} = \int_0^{s_{th}} f_{S_k|m_k=0, N_k=n}(s)ds$$
$$\approx Q\left(\frac{A^2 T_b - \sqrt{S_{th}}}{A\sqrt{\frac{4n^2+10n+7}{2}} T_b \tau_c}\right) \quad (6)$$

As identical symbol probabilities are assumed, the total bit error probability $P_{e|N_k=n}$ can be minimized with respect to s_{th} by setting $S_{th} \approx (\frac{1}{2}A \cdot T_b)^2$. Substituting the resulting conditional error probability in (3) gives

$$P_e \approx \left(\frac{1}{2}\right)^M \cdot \sum_{n=0}^{M-1} \binom{M-1}{n} \cdot \left(\exp\left(-\frac{T_b}{4(4n^2+2n)\tau_c}\right) + Q\left(\sqrt{\frac{T_b}{2(4n^2+10n+7)\tau_c}}\right)\right) \quad (7)$$

which can be numerically evaluated. Now we will compare this result to the average probability of bit error in case of balanced detection. To make a fair comparison, it should be assumed that OOK is also used in this case. Applying a similar reasoning as in the case of the phase diversity detector, the average bit error probability for balanced detection of OOK is easily found to be
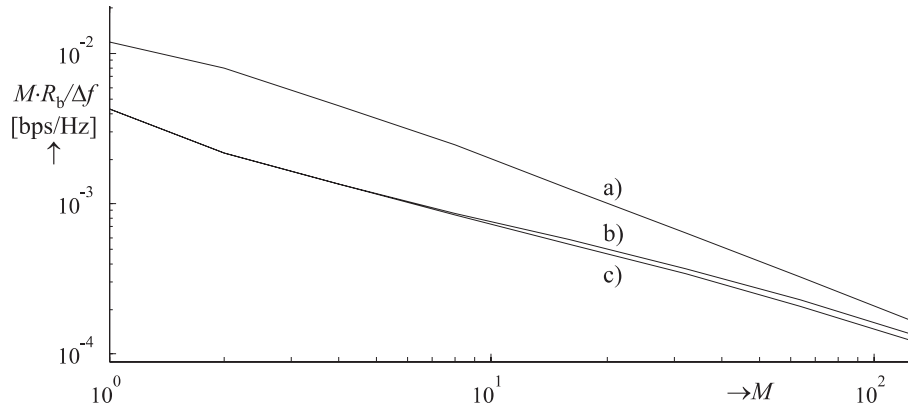
Figure 3: Network capacity over linewidth at a bit error rate $P_e = 10^{-9}$
a) BPSK modulation and balanced detection
b) OOK modulation and balanced detection
c) OOK modulation and phase diversity detection

$$P_e \approx \left(\frac{1}{2}\right)^M \cdot \sum_{n=0}^{M-1} \binom{M-1}{n} \cdot \qquad (8)$$
$$\left(Q\left(\sqrt{\frac{T_b}{2(4n^2+2n)\tau_c}}\right) + Q\left(\sqrt{\frac{T_b}{2(4n^2+10n+7)\tau_c}}\right)\right)$$

Fig. 3 shows the network capacities one can obtain for a given number of users M at an average bit-error rate of 10^{-9}. It can be verified that these results also apply to the 3×3 phase diversity receiver.

Conclusion

A phase diversity network in a CM receiver provides stabilization of the output signal without requiring phase-locking. At low bit error rates, phase diversity detection introduces only a slight capacity degradation compared to balanced detection when OOK modulation is used.

References

[1] G.J. Pendock, D.D. Sampson, "Capacity of cohe-rence-multiplexed CDMA networks", *Opt. Commun.*, vol. 143, pp. 109-117, 1997.

[2] W. van Etten, A. Meijerink, "Optical stabiliza-tion of coherence multiplex output signal by means of a phase diversity network", *Proc. Symp. IEEE/LEOS Benelux Chap.*, Brussels, Bel-gium, pp. 149-152, 2001.

[3] R.A. Griffin, D.D. Sampson, D.A. Jackson, "Demonstration of Data Transmission Using Coherent Correlation to Reconstruct a Coded Pulse Sequence", *IEEE Photon. Technol. Lett.*, Vol. 4, pp. 513-515, 1992.

[4] A.W. Davis, M.J. Pettitt, J.P. King, S. Wright, "Phase Diversity Techniques for Coherent Optical Receivers", *J. Lightwave Technol.*, Vol. 5, pp. 561-572, 1987.

CESAR: Cabauw experimental site for atmospheric research

Herman Russchenberg (1) , Fred Bosveld (2) , Daan Swart (3) , Harry ten Brink (4) , Matti Herben (5) ,
Gerrit de Leeuw (6) , Han Stricker (7) , Bertram Arbesser-Rastburg (8) , Hans van der Marel (1)
(1) Delft University of Technology, The Netherlands; correspondence: h.w.j.russchenberg@irctr.tudelft.nl
(2) Royal Netherlands Meteorological Institute, KNMI, (3) National Institute for Public Health and the
Environment, RIVM, (4) Netherlands Energy Research Foundation, ECN, (5) Eindhoven University of
Technology, TU/e, (6) Netherlands Organization for Applied Scientific Research, TNO, (7) Wageningen University
and Research Centre, WUR, (8) European Space Agency, ESA-ESTEC
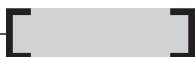
Abstract

This paper describes the contours of a national monitoring and research site for atmospheric processes related to climate change. This initiative forms the logical continuation of the collaboration between Dutch universities and research organizations in this field. The proposed station will have large benefits for atmospheric science, both in the Netherlands and internationally. Within CESAR many ground-based instruments will be operated at the Cabauw observatory in The Netherlands. The site will be unique in Europe in its overall capabilities.

Scope and research objectives of CESAR

The overall objective of the Cabauw Experimental Site for Atmospheric Research Project, hereafter referred to as CESAR Project, is:

- To set-up and operate at the Cabauw site an observational facility with a comprehensive set of remote sensing and in-situ equipment to characterize the state of the atmosphere, its radiative properties and interaction with the land surface, for the study of physical processes, climate monitoring and validation studies.

The driving motivation for this site is
1 the need for observational data to address crucial questions regarding climate change,
2 the notion that this can only be accomplished with the synergetic use of collocated remote sensing instruments in combination with in situ data,
3 the conviction that joining forces of the participating research institutes will add significant value to Dutch and international science in the field of atmospheric research.

Science background

The CESAR Project will address challenging questions in atmospheric research- especially the questions that are related to the interaction between clouds, aerosols and radiation and the land-atmosphere interface. Activities in the field of atmospheric composition- green house gases, chemical processes- will be unfolded as well.

Clouds-Aerosol-Radiation Interactions

Low-level clouds cool the earth by reflecting sunlight back into space. In contrast to that, high-level clouds tend to warm the earth by losing less infrared radiation to space. Hence, if cloud properties change or if the number of clouds changes in response to any future climate change, then the "cloud radiative feedback" can either amplify global warming or counteract it. Changes in the vertical profile of clouds lead to different heating rates and consequently to significant changes in atmospheric dynamics. Apart from the manmade greenhouse gases also manmade aerosols induce climate change by affecting the radiation balance. Low-absorbing particles (e.g., sulphate, nitrate) cool the earth by scattering incoming sunlight and thus reducing the irradinace at the Earth surface. Absorbing aerosol particles (e.g. soot from diesel engines and biomass-burning) can absorb incoming and scattered solar radiation and contribute to the warming of the atmosphere, thus reinforcing the effect of greenhouse gases. In addition to these

'direct' aerosol effects, there are 'indirect' effects associated to the role the aerosol plays in cloud formation (aerosols acting as condensation nuclei). An increase in the aerosol concentration (for instance due to human activity) can have an 'indirect' effect by (i) increasing the cloud reflection properties, and (ii) changing the cloud lifetime. This indirect effect can be as large as the warming by the extra green house gases , but the actual value is as yet, highly uncertain

Land-Atmosphere interactions

The land-atmosphere interface is a major factor in atmospheric processes. The surface energy flux directly influences growth of the planetary boundary layer, as well as terrestrial and atmospheric moisture content, cloud formation and, consequently, precipitation patterns. The surface carbon dioxide flux and its relation to vegetation and soil processes is an important factor in the global carbon cycle, and consequently to climate change. To date, atmospheric models are lacking a sufficient accurate representation of precipitation, energy surface fluxes, boundary layer dynamics and CO_2 ; the combination with soil hydrology introduces anomalies on the time scale of seasons The terrestrial hydrological balance serves as a lower boundary condition in atmospheric models. The complications to implement the lower boundary condition follow from

1. the temporal, non-linear, dynamics of the processes underlying the hydrological balance
2. the variability in spatial behaviour of these processes
3. the interactions between atmospheric and land surface processes.

Closing the hydrological balance for the area surrounding Cabauw implies measurement of spatial and temporal distributions of precipitation, soil moisture storage, evapotranspiration and discharge/seepage. Knowledge of the microstructure of precipitation (e.g. the dropsize distribution) is seen to be important information for quantifying the relevant processes.

Scientific approach

Several types of research can be distinguished: process studies, model evaluation, climate monitoring, and development of new observational techniques. For every objective, specific demands are put on the instrumentation, mode of operation and necessary infrastructure.

1. Process and model evaluation studies

For process and model evaluation studies it is crucial to observe all the relevant parameters. These will often be obtained during intensive observation periods: campaigns with a typical duration of a few weeks to several months.

2. Monitoring

The objective of monitoring is to establish the present state of the atmosphere and to detect long-term changes of the physical quantities. It requires observations over long time periods. It is planned to set up a climate-monitoring program for CESAR, involving many different instruments to measure the relevant parameters.

3. Development of new observational techniques

For reliable observations, the accuracy and reliability of the used techniques have to be determined. The testing, evaluation and improvement of observational techniques can best be done at an experimental site where independent methods are available to measure the same parameters. New retrieval algorithms, based on the synergy of sensors, can be developed for the retrieval of physical parameters with improved accuracy. Through the unique combination of sensors, it may become feasible to determine parameters that otherwise cannot be obtained.

4. Validation of satellite products

Space-based monitoring of the atmosphere has been and will be important for the detection of global changes of climate and environment, as well as for accurate weather prediction and hydrological prediction of floods and droughts. Quality assessment of the data coming from these observational platforms can only be achieved with proper validation and calibration techniques. The CESAR site offers excellent opportunities for this: the combination of in situ and remote sensing equipment will provide a comprehensive characterization of the atmospheric state that is necessary for this validation.

Implementation of CESAR

The instruments at CESAR

In Table 1 an overview is given of the instruments that are planned to be operated on the site.

The measurements at CESAR will be complemented by observations of large-scale phenomena with weather radar and satellite.

Remote sensing instruments	In-situ instruments *measurement tower*	In-situ instruments *ground based*
1 GHz wind profiler	SJAC	Rain gauges
Ir-radiometer	LAS-X	Disdrometer
Ceilometer	Optical particle counter	TDR
3 GHz radar	FSSP-95	Radiosonde
35 GHz radar	Nephelometer	Groundwater tubes
10 GHz radar	Sonic anemometer	
94 GHz radar	Infrared fluctuation meter	
Non-scanning lidar	Gas analyzer	
Raman lidar	Aethalometer	
Scanning lidar	Sun photometer	
Microwave radiometer	Humidograph	
UV radiometer	Wind sensor	
42 GHz beacon receiver	Temperature sensor	
GPS-receiver		
Scintillometer		
Pyranometer		

Table 1. Overview of the instruments that are planned at the CESAR site.

Modes of operation

Monitoring and process studies require different technical specifications of the equipment. Process studies usually encompass short-term experiments with the specifications of the equipment dedicated to details of the process under study. Process studies may also necessitate experiments during which the system specifications have to be changed. Monitoring puts other specific demands on the measurement equipment: Observations have to be made over long time periods without a change in system specifications; long-term stability is a key issue here.

The equipment at the CESAR site can be distinguished into three categories:
1. Monitoring equipment, that can be operated unattended over long periods
2. Quasi-monitoring equipment: state-of-the-art tools that require an operator during campaigns for process studies, but that can be left unattended during long term observations
3. Process study equipment: state-of-the-art tools that require an operator during campaigns and can only be used for short campaigns

The modus operandi for equipment in the quasi-monitoring mode entails observations during a fixed, well-defined percentage of time, for instance one week per month, leaving the remaining time for process studies. This will ensure a statistically reliable data set to study long-term trends, given that the observation time is long enough.

CESAR young scientists program

CESAR combines the expertise of universities and research institutes in The Netherlands. This expertise encompasses the whole field of atmospheric research: theory, experimental exploration, modeling, validation and, eventually, the application. This offers a unique chance for the training of young scientists, be it at the master, doctoral or post-doctoral level. Students from different universities with different backgrounds get the opportunity to collaborate in cutting edge projects and truly develop the appreciation for working in a multi-disciplinary environment. CESAR has the potential to become an attractive center for international young scientists to develop and deepen their skills.

Concluding remarks

A central facility for experimental atmospheric research is very important for the scientific community in The Netherlands, but also internationally. There is a large demand originating from the climate research community for comprehensive observational sites which provide observations that can be used for climate monitoring and a better understanding of the most important but hardly understood unknown climate feedbacks. The CESAR site as described in this paper would fulfil these demands. It will be a unique observational site within Europe.

CESAR will strengthen the atmospheric research community and function as a bridge between the

universities and the research institutes. The exchange of ideas between scientists from different disciplines and backgrounds will deepen and broaden science practice in The Netherlands. Furthermore, the educational potential of CESAR offers unique opportunities to young scientists.

A complete description can be downloaded from: Http://irctr.et.tudelft.nl/projects/cesar/articles/cesar_project_plan.pdf

Table 2. *Overview of the physical phenomena that can be observed with the CESAR instruments. The indicated spatial scales are: medium scale (up to 10 km); large scale (up to hundreds km)*

Instrument	Physical quantity	Sample area	scale
1 GHz wind profiler	3d wind field	3-dimensional	medium
Ir-radiometer	Intensity of infrared radiation	Integrated column	
Ceilometer	Cloud structure, cloud base	Vertical profile	medium
3 GHz radar	3d wind field, microstructure of clouds, rain structure and boundary layer processes	3-dimensional	medium
35 GHz radar	Cloud geometry, microstructure	Vertical profile	medium
10 GHz radar	Cloud geometry, microstructure, rain	Vertical profile	medium
94 GHz radar	Cloud geometry, microstructure, aerosols	Vertical profile	medium
Non-scanning lidar	Aerosols, cloud structure	Vertical profile	medium
Raman lidar	Aerosol properties , Water vapor, cloud properties, Temperature	Vertical profile	medium
Scanning lidar	Aerosols	Slant plane	medium
Microwave radiometer	Liquid water path, Water vapour path temperature profile	Integrated column Vertical profile	
UV radiometer	Intensity of UV radiation	Integrated column Slant path	
42 GHz Beacon receiver	Cloud liquid water content	Integrated column Slant path	
GPS-receiver	Horizontal water vapour distribution	2-dimensional	large
Scintillometer	Surface energy fluxes	Horizontal path	medium
Pyranometer	Radiation at several wavelengths	Integrated hemisphere	
SJAC	Aerosol size distribution	point	
LAS-X	Aerosol size distribution	point	
Optical particle counter	Aerosol size distribution	point	
FSSP-95	Aerosols/mist size distribution	point	
Nephelometer	Light scattering	point	
Sonic anemometer	Temperature and wind turbulent flux	point	
Infrared fluctuation meter	H2O and CO2 turbulent flux	point	
Gas analyzer	CO2 concentration	point	
Aethalometer	Light absorption	point	
Sun photometer	Light intensity	point	
Humidograph	Humidity	point	
Rain gauge	Rain intensity	point	Medium (1)
Disdrometer	Rain dropsize distribution	point	
TDR	Soil moisture content	point	Medium (1)
C-band weather radars	Large scale structure of rain, wind profiles and (radial) wind fields	3 dimensional	Large
Tethered balloon	Temperature, humidity, wind direction and speed	Vertical profile	
Radiosonde	Temperature, humidity, wind direction and speed	Vertical profile	

(1): in case of the foreseen network configuration

An analytic performance analysis of a class of perfectly matched layers for time-domain electromagnetcic field computation

Adrianus T. de Hoop [1], *Peter M. van den Berg* [2], *Robert F. Remis* [3]
Laboratory of Electromagnetic Research, Faculty of Information Technology and Systems,
Delft University of Technology, Mekelweg 4, 2628 CD Delft, the Netherlands,
E-mail: a.t.dehoop@its.tudelft.nl [1] *, p.m.vandenberg@its.tudelft.nl* [2] *, r.f.remis@its.tudelft.nl* [3]

Abstract

A class of Perfectly Matched Layers (PML's), characterized by an excess time delay profile and an excess absorption profile, mimicking the reflectionless radiation into a homogeneous, isotropic, lossless embedding, is introduced and their performance in the presence of a truncated layer is analyzed for a test case (transient radiation from an electric-current loop) with a completely analytic time-domain solution. The thickness of the PML and the profile steering parameters admit adjustments to guarantee a desired accuracy in the computational target region of a finite-difference or finite-element code.

Introduction

Transient electromagnetic wave propagation and scattering problems are customarily analyzed in configurations of unbounded extent. The part of the configuration in which computational time-domain methods can be used to obtain the relevant field values is, however, necessarily of bounded support. This region, the *target region*, is taken to contain those parts of the configuration in which one is interested in the detailed behavior of the field quantities involved. The target region's *embedding* in $\Re^3$ is, standardly, taken to have such simple physical properties that analytical representations can be constructed for the wave quantities in it. In principle, these representations can be employed to construct boundary relations on the outer boundary of the target region that mimic the (passive) radiation into the embedding without affecting, as far as possible, the computed field values in the target region itself. Through the construction of the embedding's Green's functions (wavefields excited by point sources of electric or magnetic volume current), the relevant boundary integral equations and Oseen's extinction theorem provide exact absorbing boundary conditions [1, Section 28.12]. Both of these relations do yield, on the target region's boundary, interrelations between the field quantities, but they do so in a non-local and non-instantaneous manner and, hence, ruin the computationally favored spatial band and explicit time structure of the algorithm (for example, the finite-difference time-domain one) for solving the relevant wave equations.

One way to preserve the computationally favored structure of the algorithm, is to construct *absorbing boundary conditions* (ABC's) that sufficiently accurately approximate the exact boundary relations by spatially local and timely instantaneous ones. Several of these are known in the literature. More recently, truncated *perfectly matched layers* (PML's) have been introduced to serve the purpose.

The performance of both ABC's and PML's is usually tested through purely numerical experiments. In such experiments the employed signatures (pulse shapes) of the sources may hide some of the features that are inherent to the approximation at hand. For a test case where the time-domain field quantities can be constructed with entirely analytical techniques the authors have carried out a performance analysis for a number of ABC's and PML's [2]; this paper also contains a number of references to the earlier literature. The present contribution focuses in more detail on a class of PML's that is characterized by an excess time delay profile and/or an excess absorption profile, where the excess profiles serve to mimic exactly the reflectionless or passive radiation into a homogeneous, isotropic, lossless embedding. The computationally required truncation of the PML gives,

however, rise to a spuriously reflected wave that disturbs the computed field values in the target region. The magnitude of this disturbance can be controlled by the steering parameters in the excess time delay and excess absorption profiles. Owing to the fact that the expressions for the field values of the spuriously reflected wave are analytically known, the thickness of the truncated PML and its profile parameters can be selected such that a desired accuracy of the computed result in the target region can be guaranteed.

The test configuration

As test configuration we take an electric current carrying wire in the shape of a small planar loop that emits transient electromagnetic radiation into a homogeneous, isotropic medium with permittivity ε and permeability μ. The barycentre of the loop is located at $\{x = 0, y = 0, z = h > 0\}$, where $\{x, y, z\}$ are the coordinates with respect to an orthogonal, right-handed, Cartesian reference frame. The vectorial area of the loop is $A = Ai_z$, where i_z is the unit vector in the z-direction (Fig. 1). Let $I = I(t)$ be the electric current in the loop, with t the time coordinate. Then, the electric field strength E and the magnetic field strength H of the emitted electromagnetic field are given by ([1], Section 26.10)

$$E = -\mu \partial_t \nabla \times F, \quad H = \nabla(\nabla \cdot F) - c^{-2}\partial_t^2 F, \qquad (1)$$

where $F = Fi_z$, with

$$F = \frac{AI(t - R_0/c)}{4\pi R_0} \text{ in which}$$

$$R_0 = [r^2 + (z-h)^2]^{1/2} \geq 0 \text{ and } r^2 = x^2 + y^2. \qquad (2)$$

Here, $AI(t)$ is the magnetic moment of the loop antenna and R_0 is the distance from the barycenter of the loop to the point of observation.

To have the radiation by this loop antenna serve as a test problem in the performance analysis of a PML, we provide the half-space $\{z < 0\}$ with the

Figure 1: Test configuration: radiating loop antenna with perfectly matched layer in {z < 0}, truncated at {z = −d}.
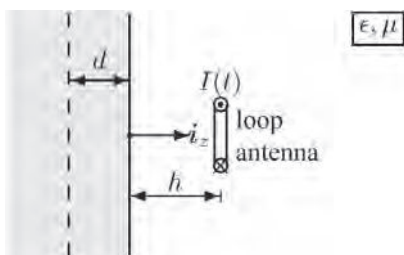
properties of such a layer. We shall carry out the construction of a rather general class of PML's through a time-domain coordinate stretching procedure. The starting point of this procedure is the partial differential equation satisfied by F, viz.

$$(\partial_x^2 + \partial_y^2 + \partial_z^2 - c^{-2}\partial_t^2)F = -AI(t)\delta(x, y, z-h), \quad (3)$$

where $\delta(x, y, z - h)$ is the three-dimensional Dirac delta distribution operative at the point $\{x = 0, y = 0, z = h\}$.

The time-domain coordinate stretching procedure

The time-domain coordinate stretching procedure, carried out in the z-direction, consists of making, in the field equations, the following replacements:

$$\partial_x \to \partial_x, \ \partial_y \to \partial_y, \ \partial_z \to \mathcal{X}_z^{-1}(z,t) \overset{(t)}{*} \partial_z, \qquad (4)$$

$$\delta(x, y, z-z') \to \delta(x, y, z-z')\mathcal{X}_z^{-1}(z,t) \overset{(t)}{*},$$

where $\mathcal{X}_{z1}^{-1}(z,t)$ is the inverse of the z-coordinate, *stretching function* $\mathcal{X}_z(z, t)$ of the layer [3,4], i.e., $\mathcal{X}_z^{-1}(z,t) \overset{(z,t)}{*} \mathcal{X}_z(z,t) = \delta(t)$ for all $z \in \mathcal{R}$. To comply with the condition that the field in the half-space $\{z > 0\}$ (which is considered to be the target region of computation) should not be disturbed by the presence of the PML, we subject the stretching function to the condition $\mathcal{X}_z(z, t) = \delta(t)$ for $z > 0$. Furthermore, the stretching function should satisfy the condition that the modified field equations in the configuration consisting of { target region} $\cup$ PML admit solutions that are uniquely determined by the excitation at hand, appropriate continuity conditions at interfaces and the property of causality in time. These aspects are most conveniently covered by an analysis in the time Laplace-transform domain.

The coordinate stretching procedure in the time Laplace-transform domain

Assuming that the exciting electric current is switched on at the instant $t = 0$, the causal time Laplace transform $\hat{I} = \hat{I}(s)$ of $I = I(t)$ is given by

$$\hat{I}(s) = \int_{t=0}^{\infty} \exp(-st)I(t)dt \text{ with } s \in \mathcal{R}, s > 0. \qquad (5)$$

We take the Laplace transform parameters s to be real and positive. (This implies that for the reconstruction of $I(t)$ from $\hat{I}(s)$ we have to rely on Lerch's uniqueness theorem [5], since the standard Bromwich inversion integral would require complex

values of s). Correspondingly, assuming zero-value initial conditions on the field quantities,

$$\hat{F}(x,y,z,s)=\int_{t=0}^{\infty}\exp(-st)F(x,y,z,t)\mathrm{d}t. \qquad (6)$$

Since under the transformation $\hat{\partial}_t = s$, $\hat{F}$ satisfies the modified Helmholtz equation

$$(\partial_x^2+\partial_y^2+\partial_z^2-s^2/c^2)\hat{F}=-A\hat{I}(s)\delta(x,y,z-h), \qquad (7)$$

while the application of the shift rule to (2) leads to

$$\hat{F}=A\hat{I}(s)\frac{\exp(-sR_0/c)}{4\pi R_0}. \qquad (8)$$

On account of (4), the z-coordinate stretched differential equation satisfied by the coordinate stretched counterpart $\hat{F}^\pi$ of $\hat{F}$ follows as

$$\left\{\partial_x^2+\partial_y^2+\frac{1}{\hat{\mathcal{X}}_z(z,s)}\partial_z\left[\frac{1}{\hat{\mathcal{X}}_z(z,s)}\partial_z\right]-\frac{s^2}{c^2}\right\}\hat{F}^\pi$$
$$=-A\hat{I}(s)\frac{1}{\hat{\mathcal{X}}_z(z,s)}\partial(x,y,z-h). \qquad (9)$$

To comply with the condition that the field equations in the stretched-coordinate domain admit causal solutions, we now assume that $\hat{\mathcal{X}}_z(z,s)$ is, for all z, a function of s that is regular in some right half of the complex s-plane, bounded as $|s|\to\infty$ in this half-plane, and real and positive at the real s-axis in this half-plane. (Note that these conditions are the same as those applying to the transfer functions of linear, passive, time-invariant systems.) The solution of (9) that is bounded as $(x^2+y^2+z^2)^{\frac{1}{2}}\to\infty$ (condition of causality) is then given by

$$\hat{F}^\pi=A\hat{I}(s)\frac{\exp(-s\hat{R}_0^\pi/c)}{4\pi\hat{R}_0^\pi}$$
$$\text{with } \hat{R}_0^\pi=[r^2+\hat{Z}(z,h,s)^2]^{\frac{1}{2}} \qquad (10)$$

$$\text{and } \hat{Z}(z,z',s)=\int_{\zeta=z'}^{z}\hat{\mathcal{X}}_z(\zeta,s)\mathrm{d}\zeta.$$

Here, $\hat{Z}$ is the s-domain PML stretched z-coordinate from z' to z. Owing to the condition that $\hat{\mathcal{X}}(z,s)=1$ for $z>0$, $\hat{F}^\pi$ reduces to $\hat{F}$ in the half-space $\{z>0\}$, which implies that the perfectly matched layer in the half-space $\{z<0\}$ as such does not influence the original wavefield in the target region $\{z>0\}$.

Excess time-delay and excess absorption PML profiles

The class of PML's whose performance we are going to analyze further has profiles of the type

$$\hat{\mathcal{X}}_z(z,s)=1+N(z)+s^{-1}\sigma(z), \qquad (11)$$

which implies

$$\mathcal{X}_z(z,t)=[1+N(z)]\delta(t)+\sigma(z)H(t) \text{ and} \qquad (12)$$

$$\mathcal{X}_z^{-1}(z,t)=\frac{1}{1+N(z)}\delta(t)-\frac{\sigma(z)}{[1+N(z)]^2}\exp\left[-\frac{\sigma(z)}{1+N(z)}t\right]H(t),$$

where $H(t)$ denotes the Heaviside unit step function. In these expressions the *excess time-delay profile* $N=N(z)$ and the *excess absorption profile* $\sigma=\sigma(z)$ are non-negative functions of z for $z<0$ and vanish for $z>0$. (Note that such $\hat{\mathcal{X}}_z(z,s)$, and correspondingly $\mathcal{X}(z,t)$, satisfy the conditions for causality.) Substitution of (11) in (10) leads to

$$\hat{F}^\pi=sA\hat{I}(s)\hat{G}^\pi \text{ in which}$$
$$\hat{G}^\pi=\frac{1}{4\pi R_d}\frac{\exp\left\{-T_d[(s+\Gamma)^2+\Omega^2]^{\frac{1}{2}}\right\}}{[(s+\Gamma)^2+\Omega^2]^{\frac{1}{2}}} \text{ for } R_d\neq0, \qquad (13)$$

with

$$Z_d=\int_{z'}^{z}[1+N_z(\zeta)]\mathrm{d}\zeta, \quad Z_a=\int_{z'}^{z}\sigma_z(\zeta)]\mathrm{d}\zeta,$$
$$R_d=(r^2+Z_d^2)^{\frac{1}{2}}\geq0, \quad Td=R_d/c,$$
$$R_a=(r^2+Z_a^2)^{\frac{1}{2}}\geq0, \quad \Gamma=Z_dZ_a/R_d^2,$$
$$\Omega=(R_a^2/R_d^2-\Gamma^2)^{\frac{1}{2}}\geq0. \qquad (14)$$

The time-domain equivalent of (13) is [6]

$$F^\pi=\partial\left[AI(t)\overset{(t)}{*}G^\pi\right]$$

in which

$$G^\pi=\frac{\exp(-\Gamma t)}{4\pi R_d}J_0\left[\Omega(t^2-T_d^2)^{\frac{1}{2}}\right]H(t-T_d)$$

$$\text{for } R_d>0, \qquad (15)$$

where J_0 is the Bessel function of the first kind and order zero. From this it is clear that T_d is the travel time of the coordinate-stretched wave function from the source point to the point of observation, Γ is the attenuation that the wave undergoes during its passage, while Ω is the angular frequency of oscillation induced by the coordinate stretching procedure.

The PML truncation generated spuriously reflected wave

To investigate the influence of a (computationally required) truncation of the PML, we determine the vector potential $F^{r;\pi}$ of the spuriously reflected wave generated by a planar boundary at $z=-d$, with $d>0$, on which the tangential electric field strength vanishes, i.e., $F^\pi+F^{r;\pi}=0$ as $z\downarrow-d$. Application of the method of images leads to
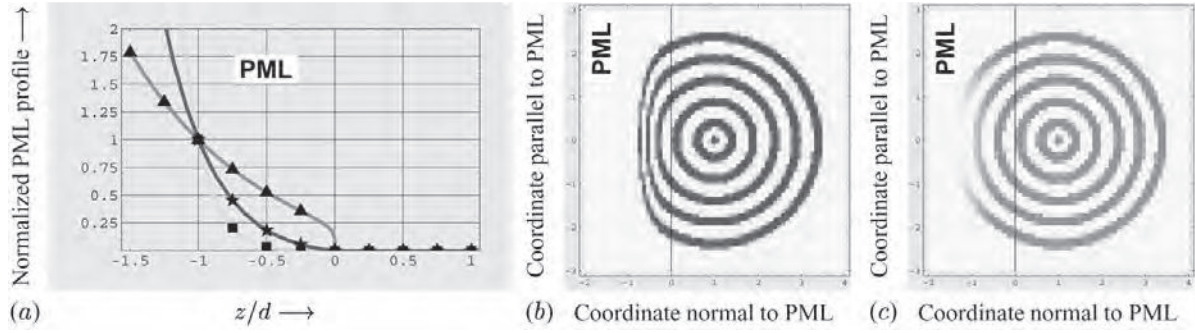
Figure 2: (a) Normalized PML excess time-delay and absorption profiles (▲ ———— $A = 1.0$, $\nu = 0.5$, $\beta = 1.0$; ■ ———— $A = 1.0$, $\nu = 2.0$, $\beta = 4.0$; ★ ———— $A = 1.0$, $\nu = 1.0$, $\beta = 2.0$; (b) Wavefronts at successive time intervals in configuration with excess time delay PML ($A_N = 4.0$, $\nu_N = 1.0$, $\beta_N = 1.0$, $A_\sigma = 0$); (c) Wavefronts at successive time intervals in configuration with excess absorption PML ($A_\sigma = 4.0$, $\nu_\sigma = 1.0$, $\beta_\sigma = 1.0$, $A_N = 0$).

$$\hat{F}^{r;\pi} = -\frac{A\hat{I}(s)}{4\pi\hat{R}_2^\pi}\exp[-(s/c)\hat{R}_2^\pi] \quad \text{for} \quad z > -d, \quad (16)$$

in which

$$\hat{R}_2^\pi = [r^2 + \hat{Z}_2^2]^{\frac{1}{2}} \quad \text{with}$$

$$\hat{Z}_2(z,d,h,s) = \int_{\xi=-(2d+h)}^{z} \hat{\mathcal{X}}_z'(\xi,s)\mathrm{d}\xi. \quad (17)$$

Here $\hat{\mathcal{X}}_z'$ is the s-domain PML profile symmetrized about the plane $\{z = -d\}$ of truncation and $\hat{Z}_2$ is the s-domain PML stretched coordinate normal to the layer from the image of the source in the truncation plane to the point of observation in the half-space $\{z \geq 0\}$. Transformation of (16) back to the time domain yields the expression for $F^{r;\pi} = F^{r;\pi}(x,y,z,t)$. PML profiles characterized by an excess time-delay constituent and an excess absorption constituent, lead to an expression for $F^{r;\pi}$ of the type (15), in which the stretched coordinate quantities now apply to the path traversed from the image of the source to the point of observation via the symmetrized profile with the plane $\{z = -d\}$ as the plane of symmetry.

Some fully analytically amenable examples

Illustrative examples have been worked out for profiles of the type

$$\{N(z), \sigma(z)\} = \{A_{N,\sigma}(-z/d)^{\nu_{N,\sigma}}\exp[-\beta_{N,\sigma}(z+d)], 0\}$$
$$\text{for } \{-d < z < 0, z > 0\}, \quad (18)$$

where $A_{N,\sigma}$, $\nu_{N,\sigma}$ and $\beta_{N,\sigma}$ are real-valued, non-negative parameters. At the reference plane $\{z = -d\}$, these profiles have the value $A_{N,\sigma}$, while they are continuous across the plane $\{z = 0\}$ where the PML starts. This continuity requirement seems to be preferred in computational implementations,

although our analysis does not require it. The value of $\nu_{N,\sigma}$ determines the behavior near $\{z = 0\}$, the value of $\beta_{N,\sigma}$ determines the behavior as $z \to -\infty$. Figure 2a illustrates this. Figure 2b shows how the propagation of the disturbance into the PML with excess time delay is slowed down. Figure 2c indicates how the disturbance is attenuated with increasing depth in the PML. All the different steering parameters in (18) are at one's disposal to construct PML's with a guaranteed time delay and/or attenuation in the computational target region.

REFERENCES
[1] A. T. de Hoop, *Handbook of Radiation and Scattering of Waves*. London: Academic Press, 1995.
[2] A.T. de Hoop, P. M. van den Berg, and R. F. Remis, "Absorbing Boundary Conditions and Perfectly Matched Layers - An analytic time-domain performance analysis," in press *(IEEE Transactions on Magnetics, May, 2002)*.
[3] W. C. Chew, W. M. Jin, and E. Michielssen, "Complex coordinate stretching as a generalized Absorbing Boundary Condition," *Microwave and Optical Technology Letters*, vol. 15, pp. 599-604, 1997.
[4] M. Kozuoglu and R. Mittra, "A systematic study of Perfectly Matched Absorbers," in: *Frontiers in Electromagnetics*, D. H. Werner and R. Mittra, Eds. New York: IEEE Press, Chapter 14, 2000.
[5] D. V. Widder, *The Laplace Transform*. Princeton University Press, p. 63, 1946.
[6] M. Abramowitz and I. A. Stegun, *Handbook of Mathematical Functions*. New York: Dover Publications, p.1027, 1965.

Aankondigingen & Oproepen

Excursie naar Delphi Automotive Systems,
Wuppertal, Duitsland.

Mededeling van de Programmacommissie van het NERG.

De programmacommissie is doende voor de komende herfst een themamiddag te wijden aan elektronica in auto's. Het is nog niet zover dat wij U al een spreker en een datum voor dit onderwerp kunnen aanbieden maar in hetzelfde verband hebben we wel de mogelijkheid één van de, tot de *DELPHI Automotive Systems* behorende ontwikkeling- en fabricagecenters te bezoeken. De Delphi onderneming heeft zijn basis in de Verenigde Staten van Amerika en op de website www.delphi.com kunt U ermee kennismaken.

De excursie die wij nu kunnen organiseren geldt een bezoek aan de Delphi vestiging in Wuppertal (D) waar men ons een programma aan wil bieden waarin een aantal elektronicatoepassingen in auto's zal worden toegelicht en het bedrijf zal worden bezichtigd.

Delphi werkt voor haar ontwikkelingswerk nauw samen met de auto-industrie en houdt zich o.a. bezig met Engine management, Fuel injection, Exhaust control,

Traffic control by satellite Global Position System. Deze laatste toepassing kent ook een "Red Button" die in geval van een ongeluk ingedrukt kan worden en de gegevens omtrent de positie van de auto dan aan een centrale doorgeeft. In de Entertainment sector zijn er ontwikkelingen op het gebied van radio en TV en spraakherkenning voor gebruik in auto's.

Wij doen deze mededeling nu om vast te kunnen stellen of er voldoende belangstelling is voor een dergelijke excursie. De datum van het bezoek is al vastgesteld en is woensdag 4 december a.s. Gedacht wordt om ca.11 uur in Wuppertal aan te komen. Het programma zal tot tegen het einde van de middag lopen.

De reismogelijkheden zijn per eigen auto of per trein. Er is een goede treinverbinding met Wuppertal. Als voorbeeld noemen wij Vertrek Utrecht 7.42 uur met aankomst Wuppertal Hbf. om 10.00 uur. Het voordeligste treinkaartje is een z.g.n. dagkaart die € 59.70 kost. Met dat kaartje

kan men dan vanuit elke plaats in Nederland heen en terug naar Wuppertal reizen. In Wuppertal zullen we, in nader overleg met Delphi, transport van het treinstation naar het bedrijf kunnen regelen.

De programmacommissie wil gaarne antwoord op de volgende vragen:

- Zal U zich t.z.t. waarschijnlijk aanmelden voor deze excursie?
- Reist U per trein of geeft U de voorkeur aan de auto?

Deze opgaven verwachten we gaarne voor 18 oktober 2002 bij voorkeur op het e-mail adres kpanne@wxs.nl.
Ook kunt U natuurlijk per post antwoorden op het adres:
Ing. C.B. van de Panne,
Bachlaan 28,
1217 BX Hilversum.

Indien de excursie doorgang vindt, zal het definitieve convocaat een duidelijke routebeschrijving bevatten.